Electronic Supplementary Information

Heterogeneous Molecular Co-N-C Catalysts for Efficient Electrochemical H₂O₂ Synthesis

Chang Liu [a], Zixun Yu [a, b], Fangxin She [a], Jiaxiang Chen [a], Fangzhou Liu [a], Jiangtao Qu [c], Julie M. Cairney [c], Chongchong Wu [d], Kailong Liu [e], Weijie Yang [e], Huiling Zheng [f], Yuan Chen [a*], Hao Li [b*], and Li Wei [a*]

a. School of Chemical and Biomolecule Engineering, The University of Sydney; Sydney, New South Wales, Australia

b. Advanced Institute for Materials Research (WPI-AIMR), Tohoku University; Sendai, Japan

c. Australian Centre for Microscopy and Microanalysis, The University of Sydney; Sydney, New South Wales, Australia

d. Department of Chemical and Petroleum Engineering, University of Calgary; Calgary, Alberta, Canada

e. School of Energy, Power and Mechanical Engineering, North China Electric Power University, Baoding, 071003 China

f. State Key Laboratory of Clean and Efficient Coal Utilization, Taiyuan University of Technology, Taiyuan 030024, China

Author email: li.hao.b8@tohoku.ac.jp (L.H.), yuan.chen@sydney.edu.au (Y.C.), l.wei@sydney.edu.au (L.W.)
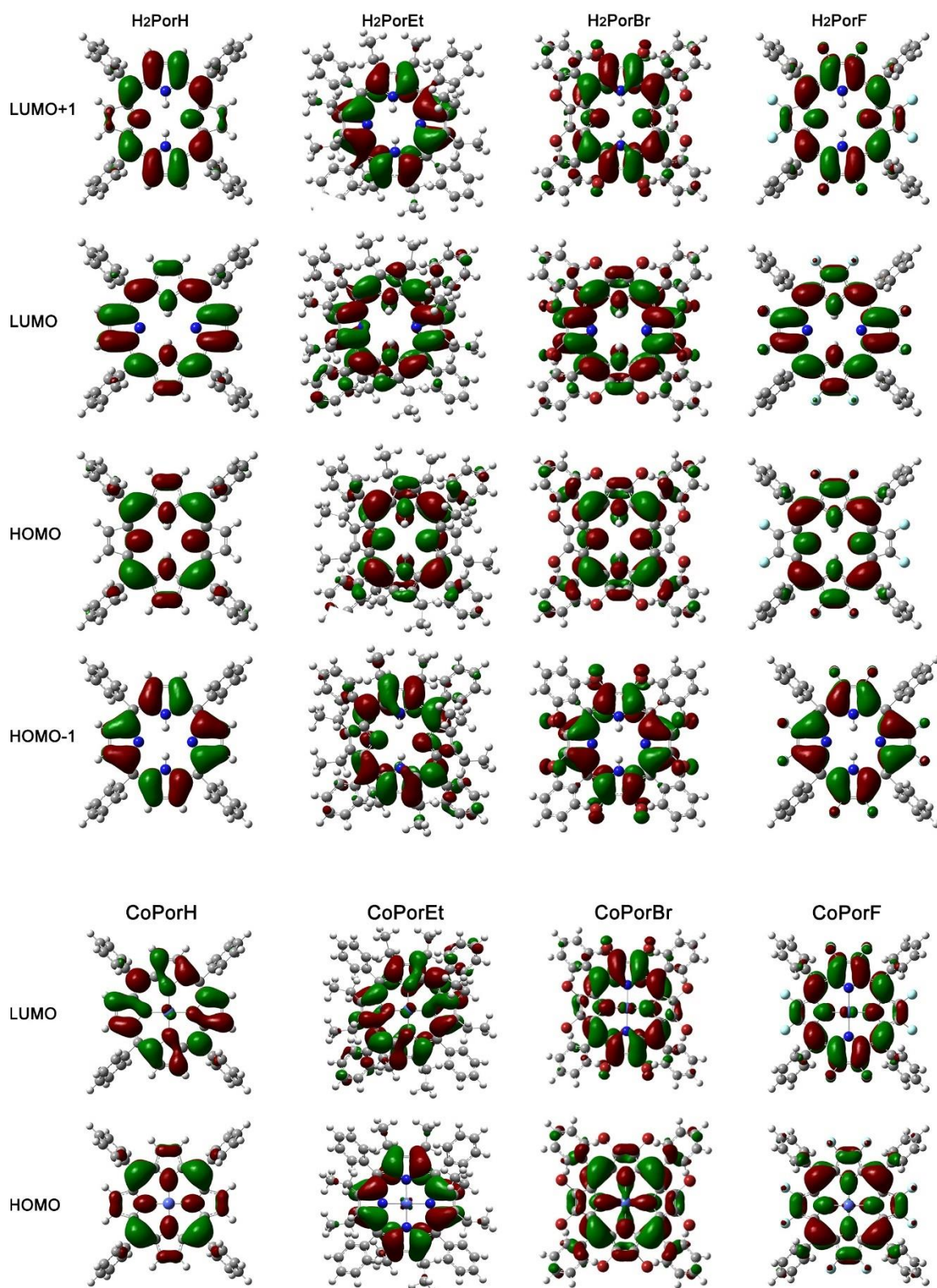
Figure S1. The calculated frontier molecular orbitals at the highest-occupied molecule orbitals (HOMO and HOMO-1) and the lowest-unoccupied molecule orbitals (LUMO and LUMO+1) of the porphyrins with β- H, Et, F, or Br substituents in their base form and metallated forms. After cobalt metallation, the improved molecular symmetry leads to degenerated molecular orbitals, reducing the energy difference between HOMO and HOMO-1, and LUMO and LUMO+1 orbitals. Grey, white, blue, and light blue spheres represent C, H, N, and Co.
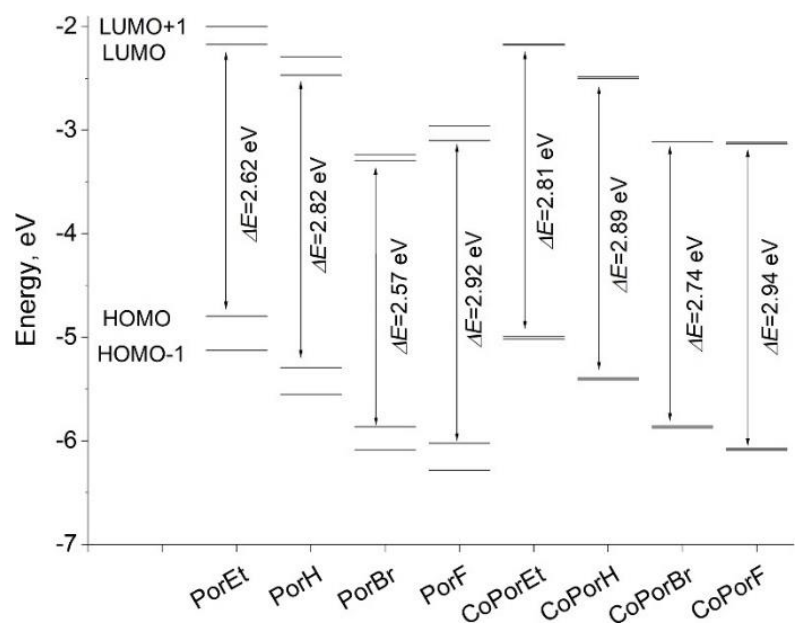
Figure S2. Calculated molecular energy structure of the porphines and cobalt porphyrins.
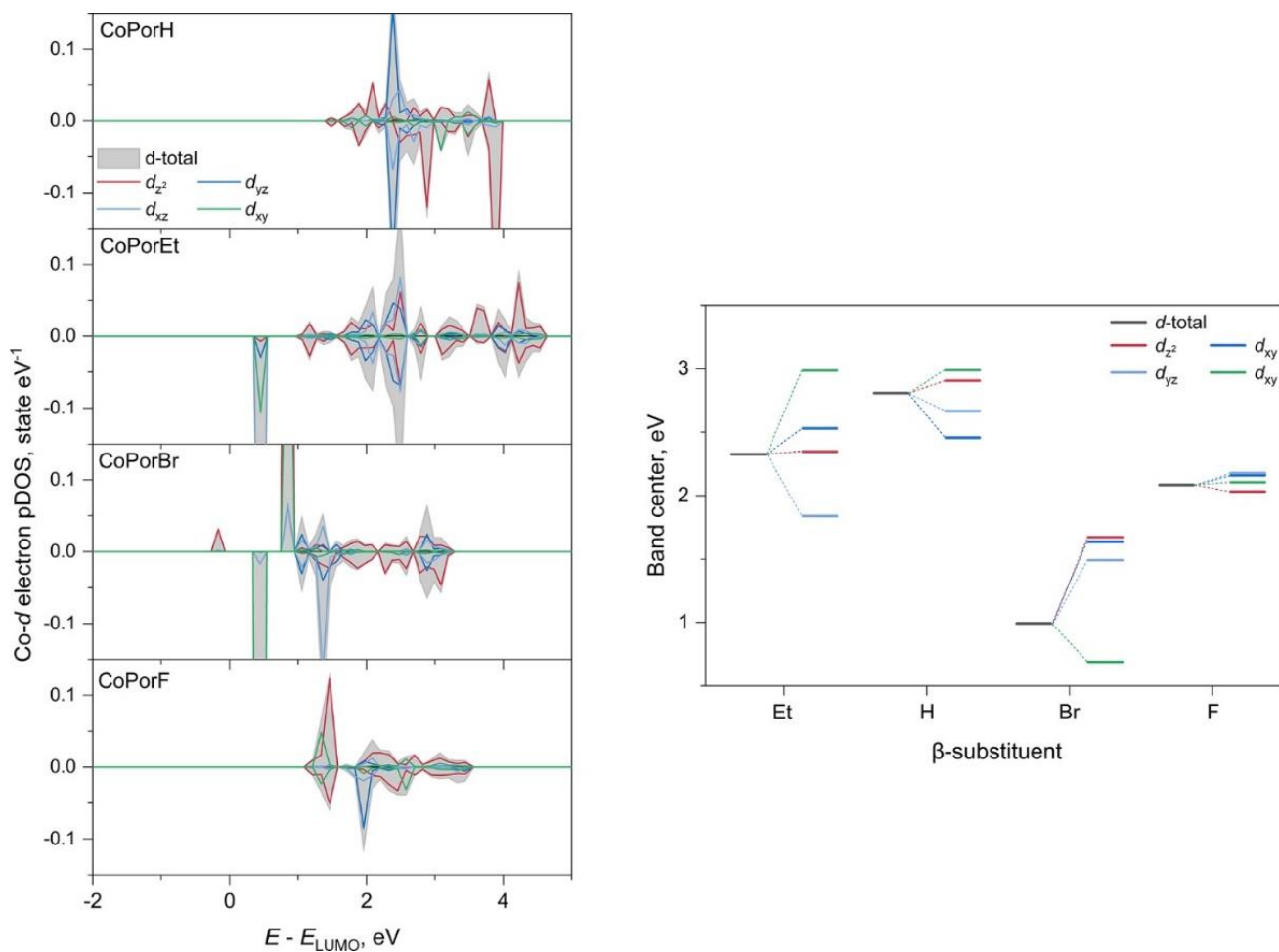
Figure S3. Calculated Co *d*-electron spin polarized pDOS and the corresponding *d*-orbital band centers of the *β*-substituted cobalt porphyrins.
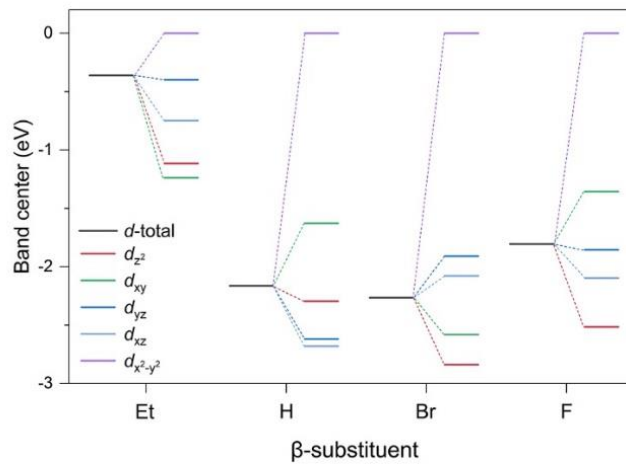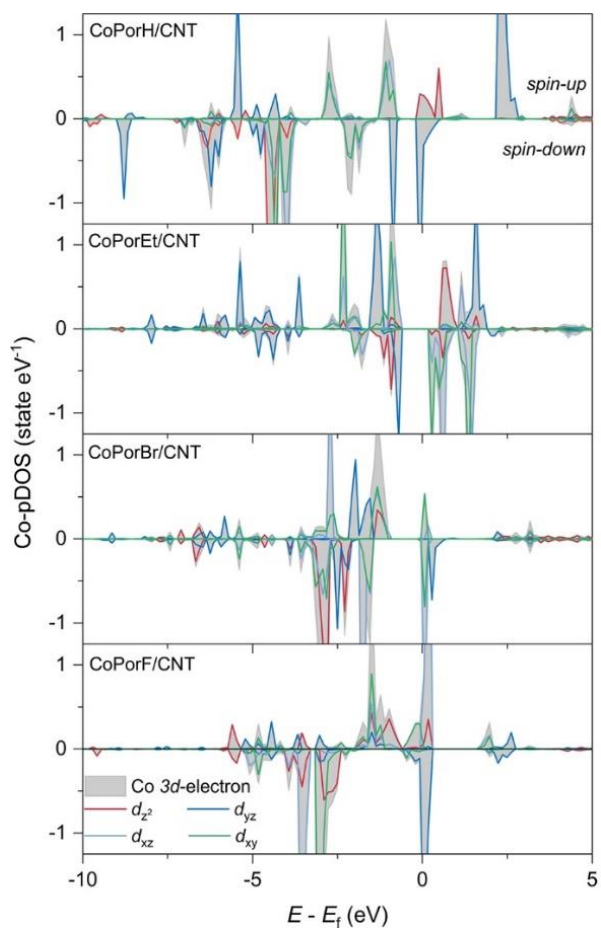
Figure S4. Calculated Co *d*-electron pDOS and the *d*-orbital band centers of the HMCs.
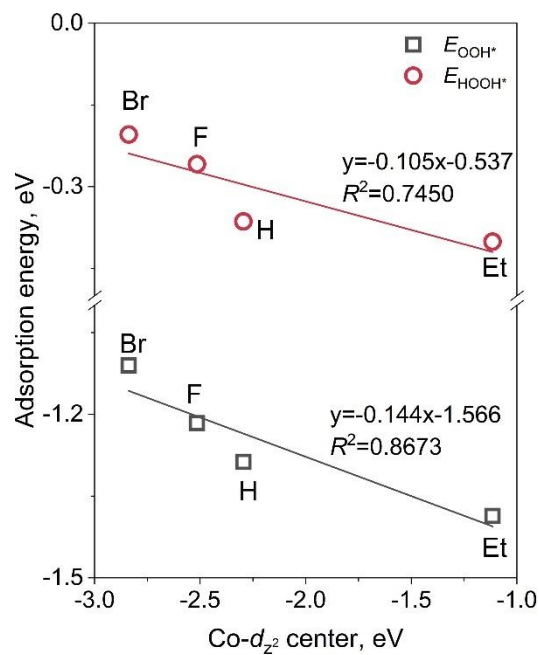
Figure S5. Trends between the calculated Co-d_{z^2} orbital center and the E_{OOH} and E_{HOOH}. The closer the Co-d_{z^2} orbital center to the Fermi level (E_F, shifted to 0 eV) would result in more negative binding energies for both *OOH and *HOOH, leading to stronger intermediates binding.
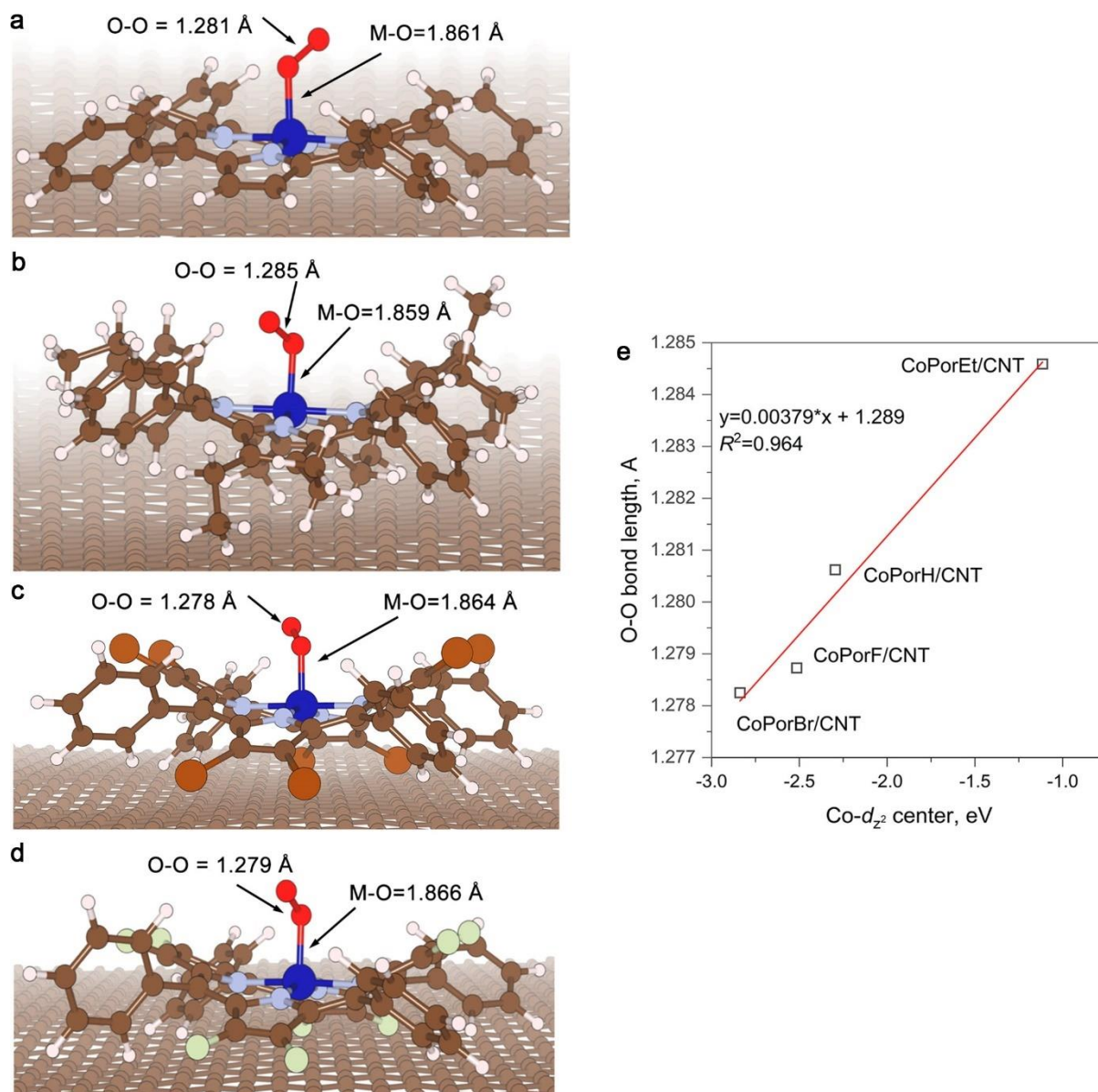
Figure S6. O_2 adsorption geometries on the (a) CoPorH/CNT, (b) CoPorEt/CNT, (c) CoPorBr/CNT, and (d) CoPorF/CNT HMC models. (e) Correlation between calculated Co-d_{z^2} orbital center and the O-O bond. Brown, pink, blue, light blue, red, light brown, and teal spheres represent C, H, N, Co, O, Br, and F, respectively.
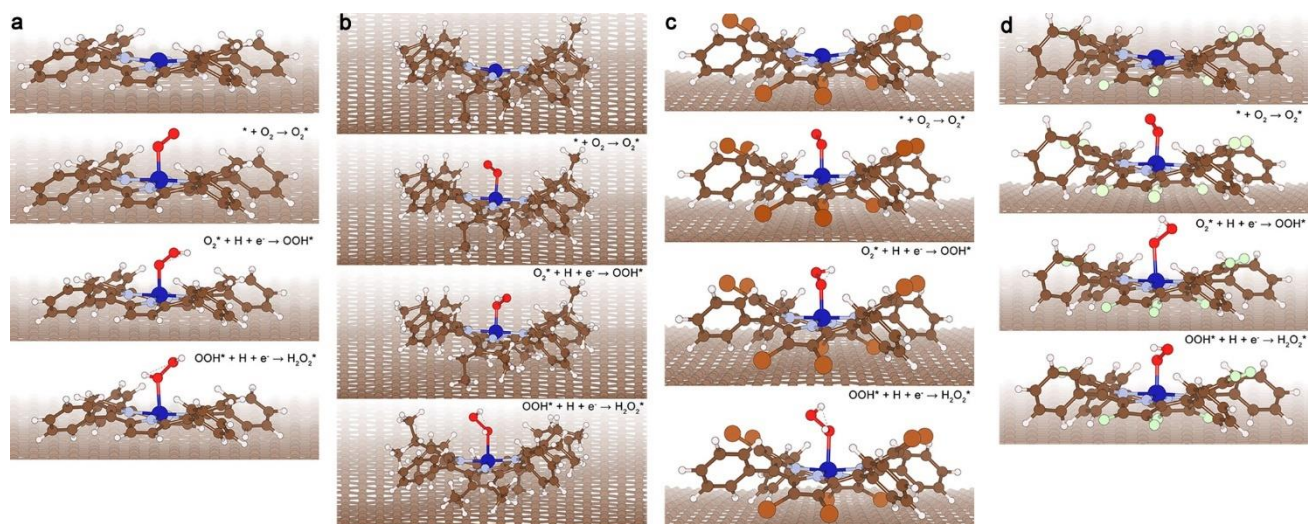
Figure S7. Adsorption geometries of various intermediates along the 2e⁻-ORR pathway on (a) CoPorH/CNT, (b) CoPorF/CNT, (c) CoPorEt/CNT, and (d) CoPorBr/CNT models. Brown, pink, blue, light blue, red, light brown, and teal spheres represent C, H, N, Co, O, Br, and F, respectively.
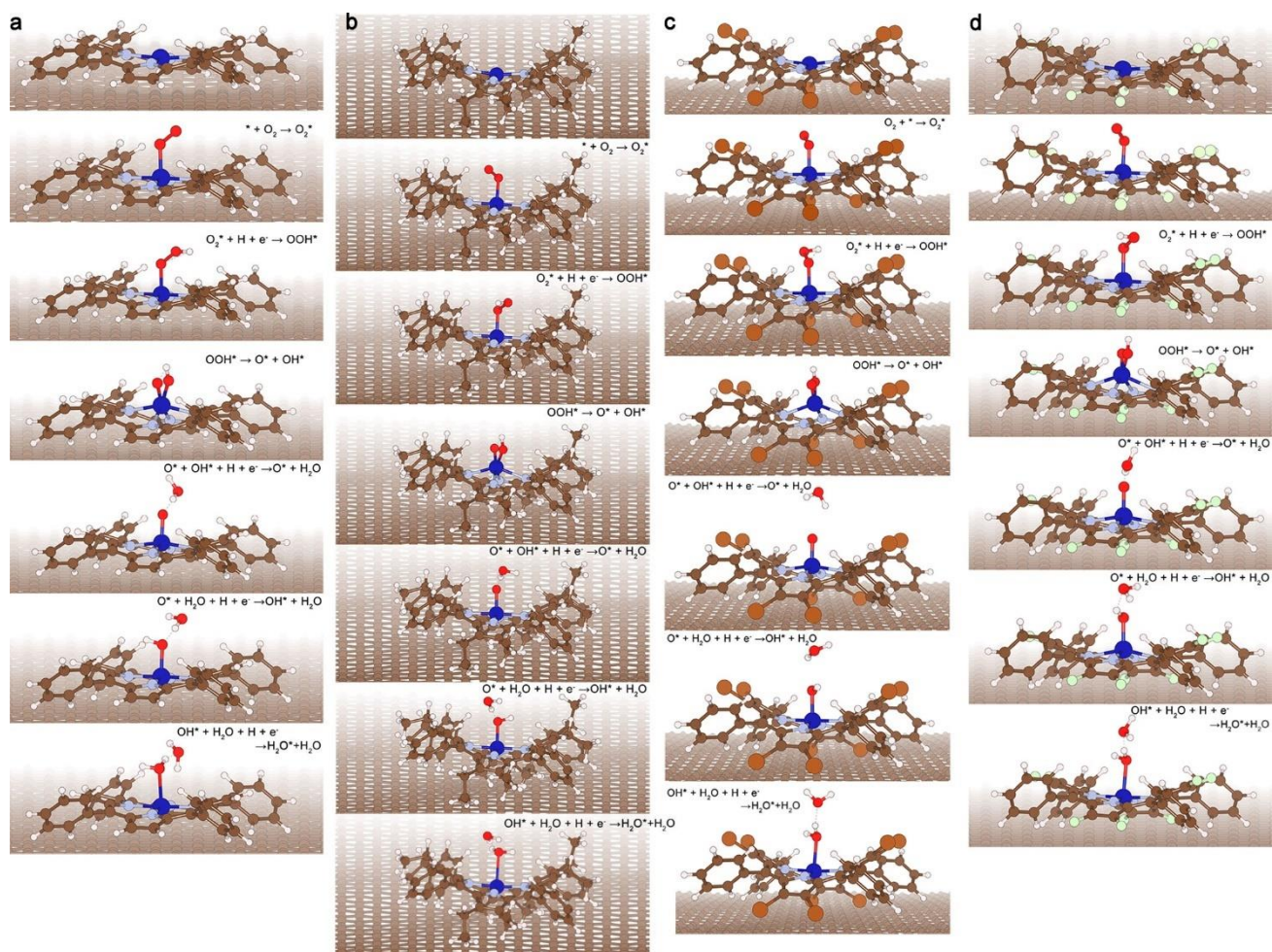
Figure S8. Optimized adsorption geometries of various intermediates along the 4e⁻-OOH dissociative pathway on (a) CoPorH/CNT, (b) CoPorEt/CNT, (c) CoPorBr/CNT, and (d) CoPorF/CNT models. Brown, pink, blue, light blue, red, light brown, and teal spheres represent C, H, N, Co, O, Br, and F, respectively.
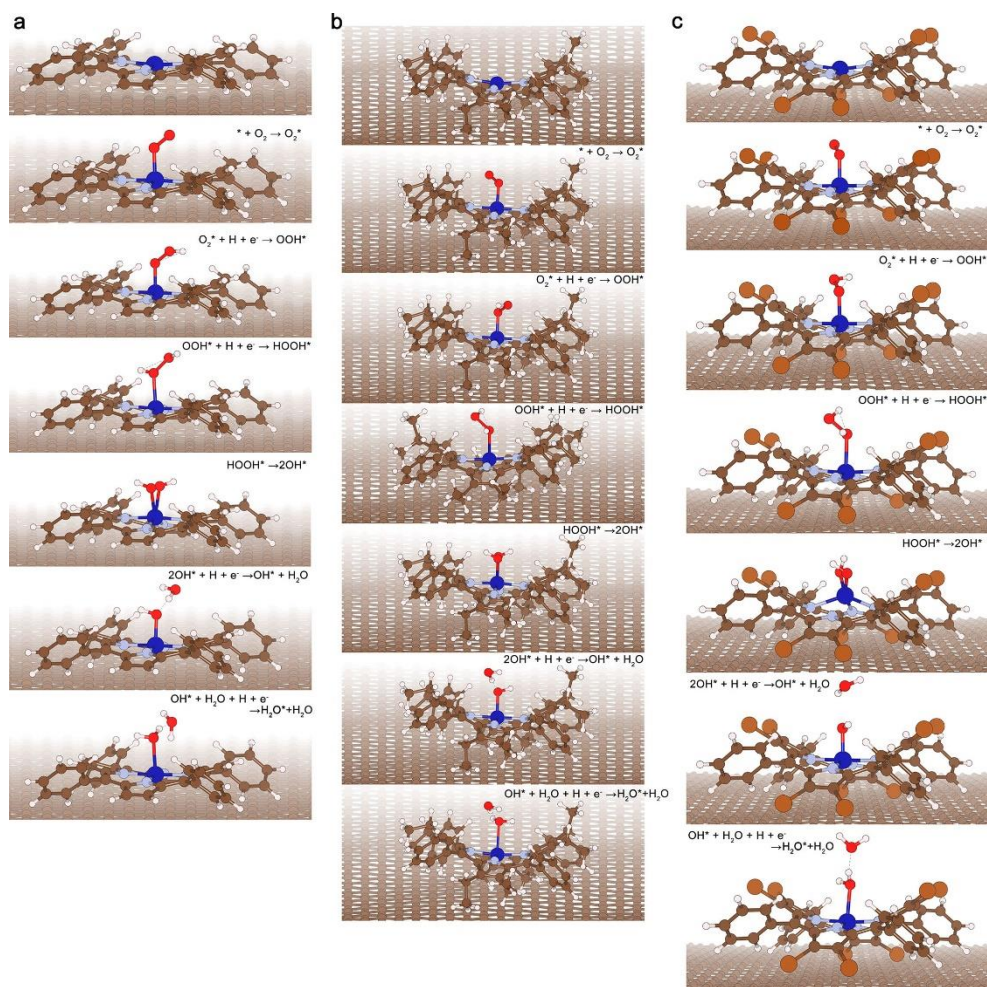
Figure S9. Adsorption geometries of various intermediates along the 4e⁻-HOOH dissociative pathway on (a) CoPorH/CNT, (b) CoPorEt/CNT, and (c) CoPorBr/CNT. Brown, pink, blue, light blue, red, and light brown spheres represent C, H, N, Co, O, and Br, respectively.
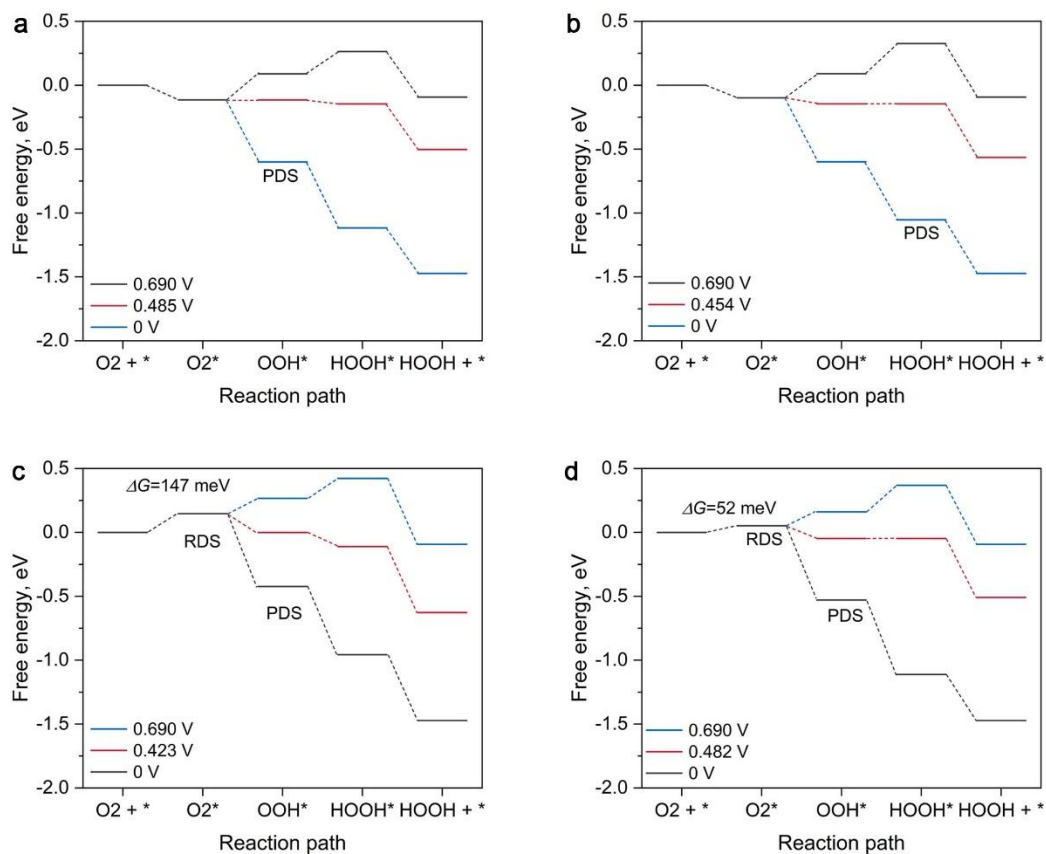
Figure S10. The free energy diagrams along the 2e⁻-ORR pathway on (a) CoPorH/CNT, (b) CoPorEt/CNT, (c) CoPorBr/CNT, and (d) CoPorF/CNT HMC models.
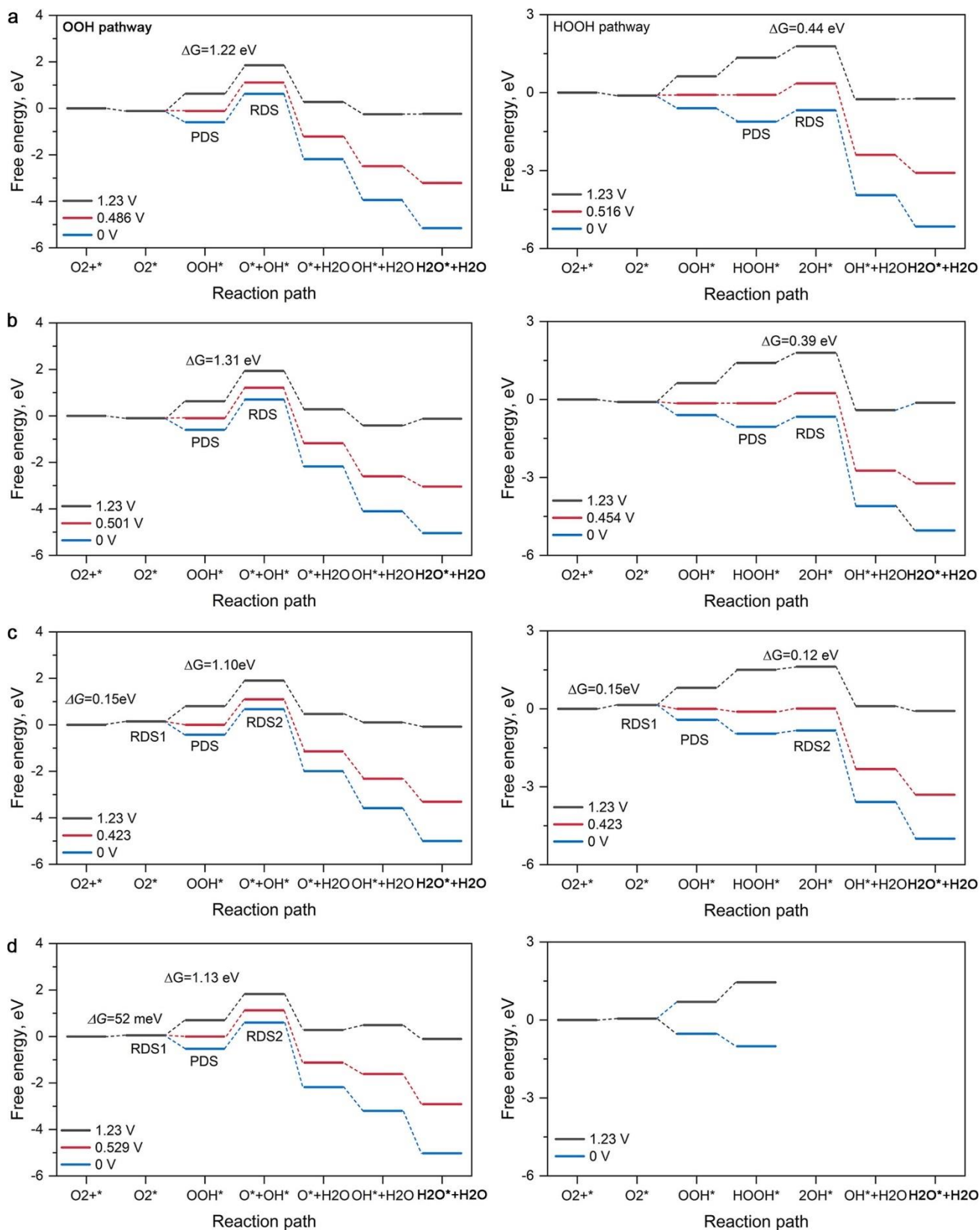
Figure S11. The free energy diagrams along the 4e⁻-ORR OOH dissociative (left panels) and 4e⁻-ORR HOOH dissociative (right panels) pathway on (a) CoPorH/CNT, (b) CoPorEt/CNT, (c) CoPorBr/CNT, and (d) CoPorF/CNT HMC models.
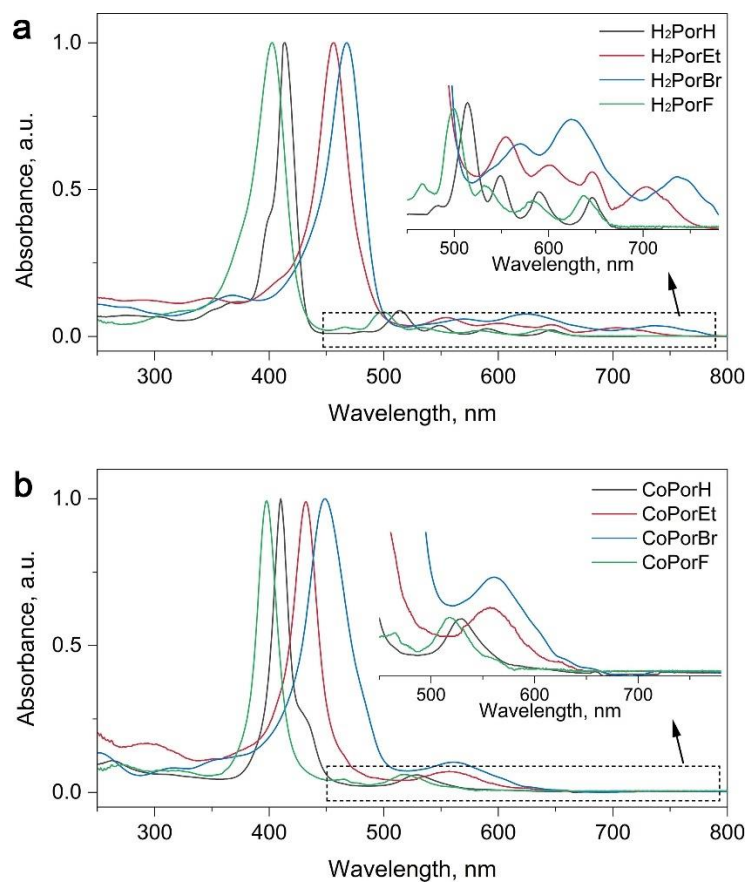
Figure S12. UV-vis spectra of the β-substituted (a) porphines and (b) cobalt porphyrins in CH_2Cl_2. Insets show the magnified Q-band region in the dashed rectangle.
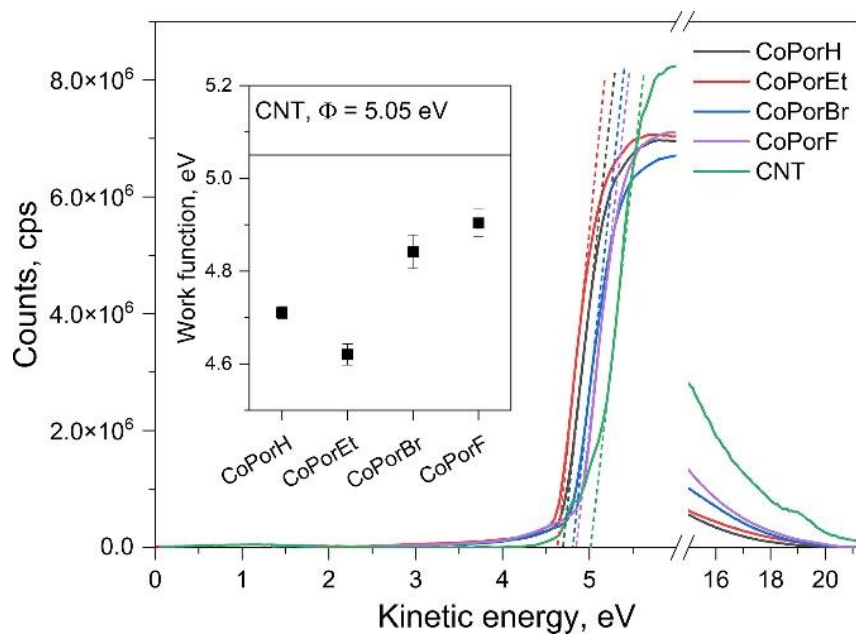
Figure S13. UPS spectra of the CNT and the cobalt porphyrins. The work functions (*Φ*) were determined from the cut-off energies were compared in the Inset.
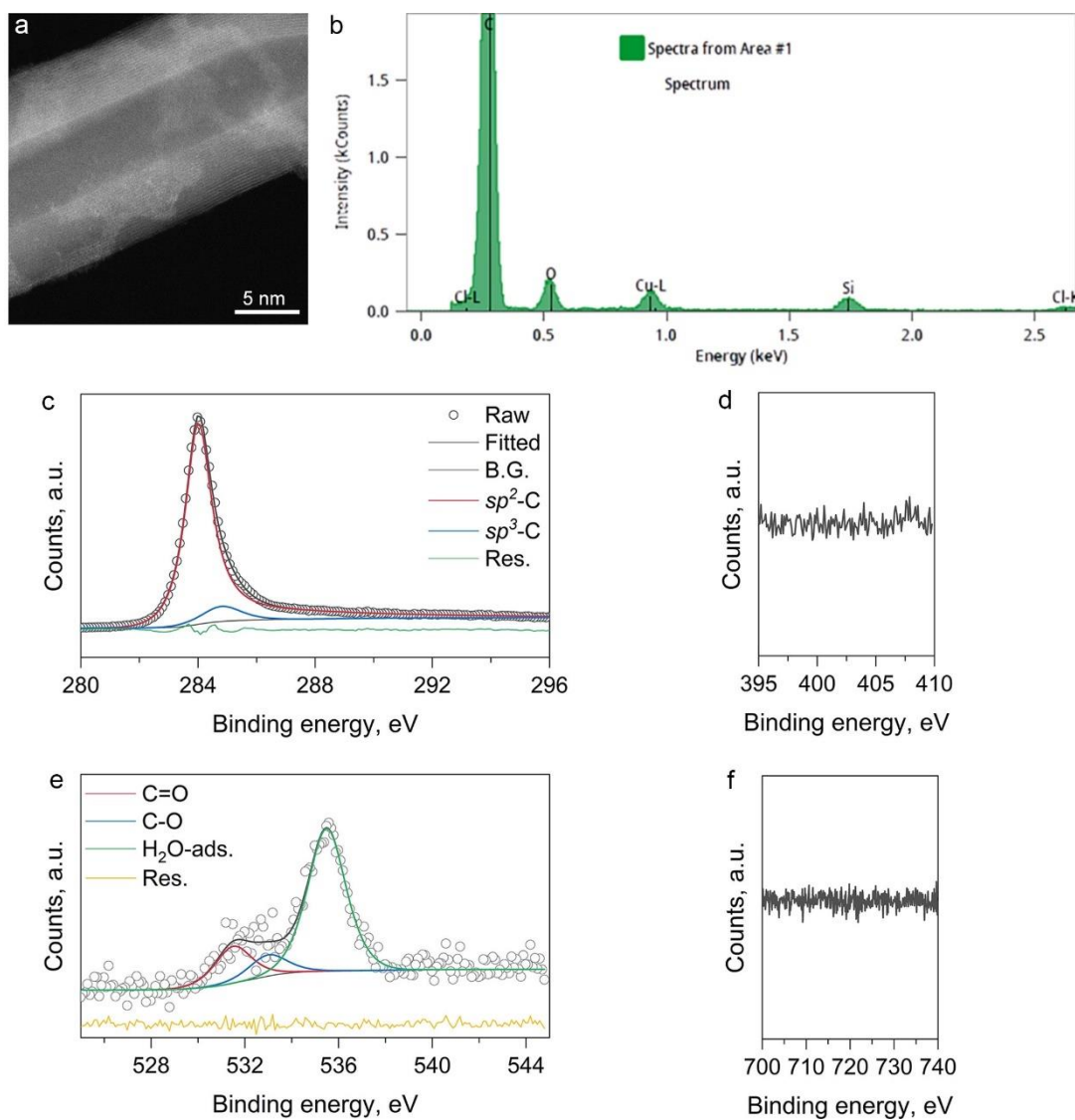
Figure S14. (a) TEM image and (b) the corresponding EDX spectrum, and the high-resolution XPS spectra of (c) C 1s, (d) N 1s, (e) O 1s, and (f) Fe 2p of the purified CNT.
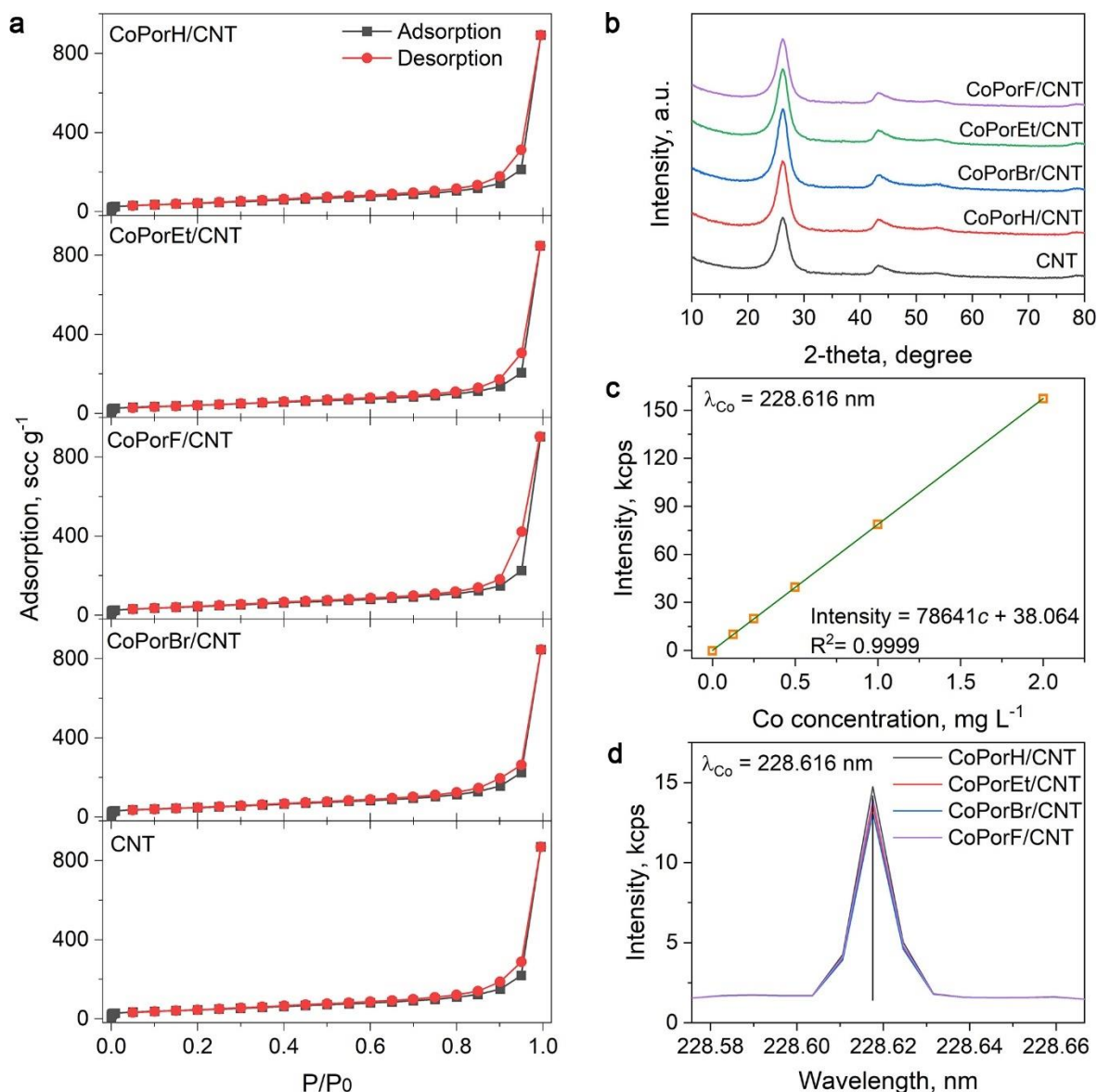
Figure S15. Physiochemical properties characterization of the HMCs. (a) N_2 physisorption isotherms and (b) XRD patterns of the catalysts and the CNT substrate. (c) ICP-AES calibration curve and (d) the Co concentration in different HMCs. The HMCs exhibit identical physisorption isotherms, affording a similar specific surface area of about 200 m^2 g^{-1}. The peaks found on their X-ray diffraction patterns (XRD) can be only assigned to the CNT substrate, suggesting the minimum presence of porphyrin aggregates.
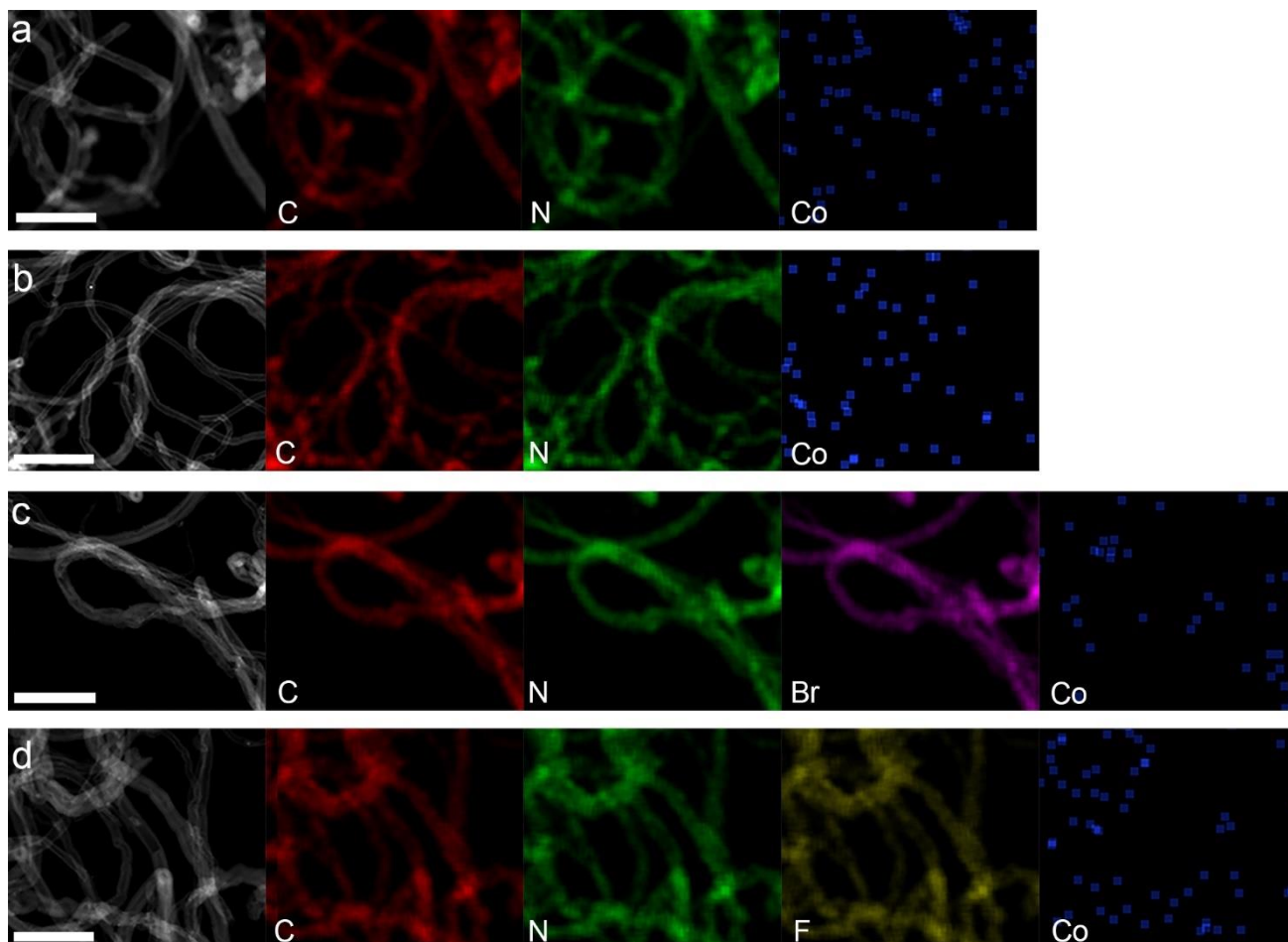
Figure S16. HADDF-STEM images and the corresponding EDX elemental mapping results of different catalysts. (a) CoPorH/CNT, (b) CoPorEt/CNT, (c) CoPorBr/CNT, and (d) CoPorF/CNT catalysts. The scale bar is 100 nm.
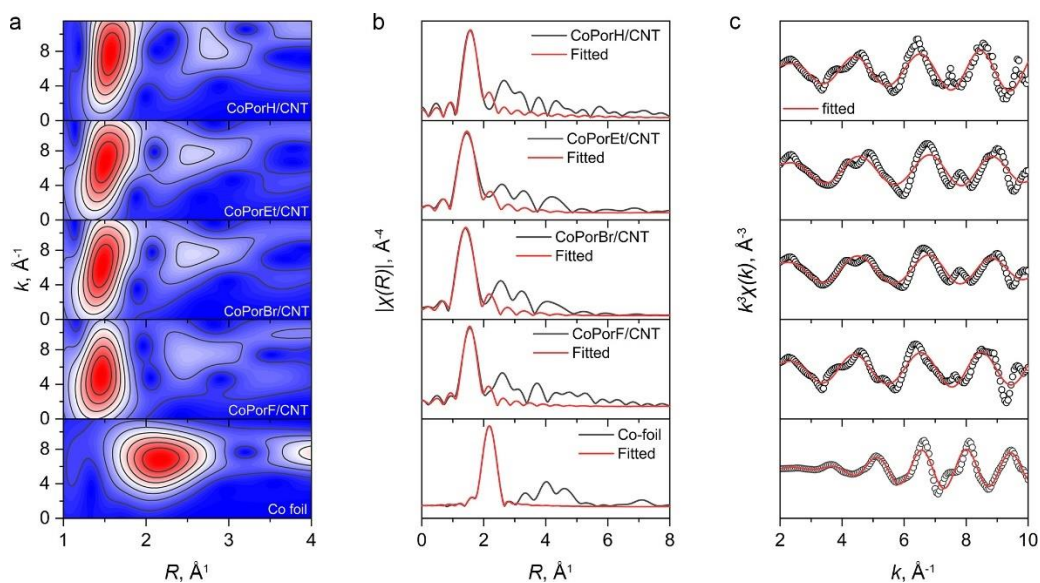
Figure S17. (a) WT-EXAFS spectra of the HMCs in comparison to that of the reference Co foil sample. A single and strong peak at ~1.5 Å can be found for all HMC samples. Compared to the Co foil reference, no Co-Co interaction at ~2.2 Å can be found. The obvious signal change in the second shell region (R between 2 to 3.5 Å) is indicative of the distorted porphyrin core structure. Fitted EXAFS in (b) R-space and (c) k-space. Fitting parameters and results are listed in the Table S6 below.
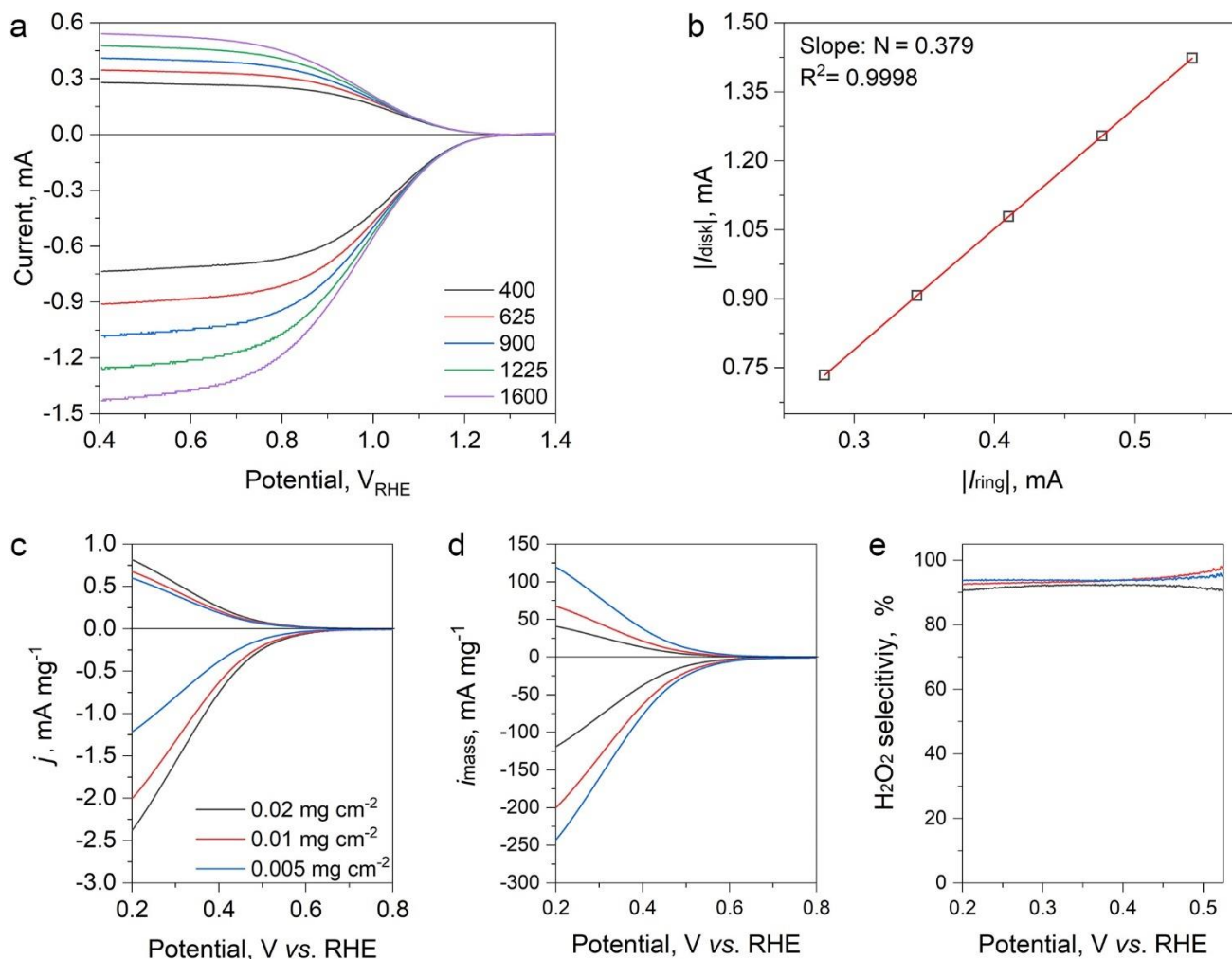
Figure S18. Electrode calibration and optimizing catalyst loading. (A) LSV curves obtained in a 0.1 M KOH electrolyte containing 1 mM $K_3[Fe(CN)_6]$ at different rotation speed. The ring potential is set at 1.5 V_{RHE}. (B) Disk current as a function of the ring current. Linear fitting affords a slope of 0.379, corresponding to a collection efficiency of .379. (C) ORR LSV curves, (D) mass specific disk-ring currents, and (E) H_2O_2 selectivity of the CoPorF/CNT catalyst measured in 0.1 M ABS at different mass loading of 5, 10 and 20 μg cm^{-2}.
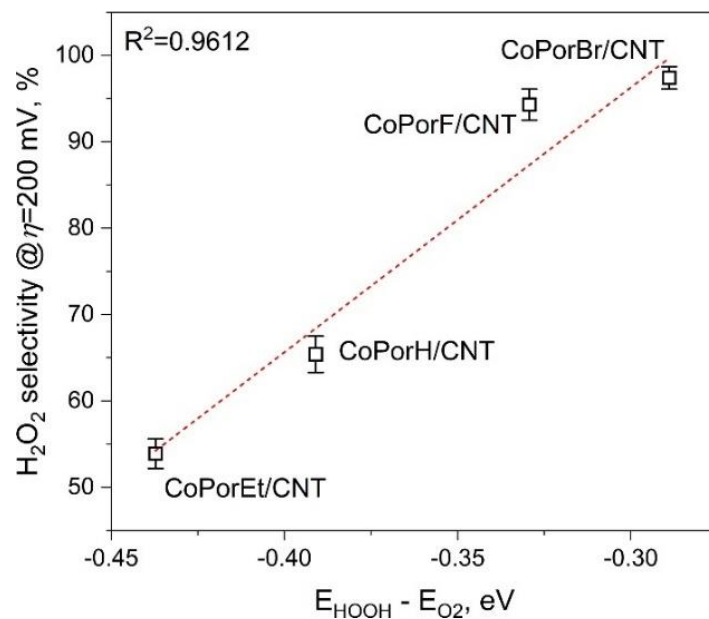
Figure S19. Correlation between H_2O_2 selectivity and the binding energy difference between O_2 and HOOH intermediates ($\Delta E = E_{HOOH} - E_{O2}$).
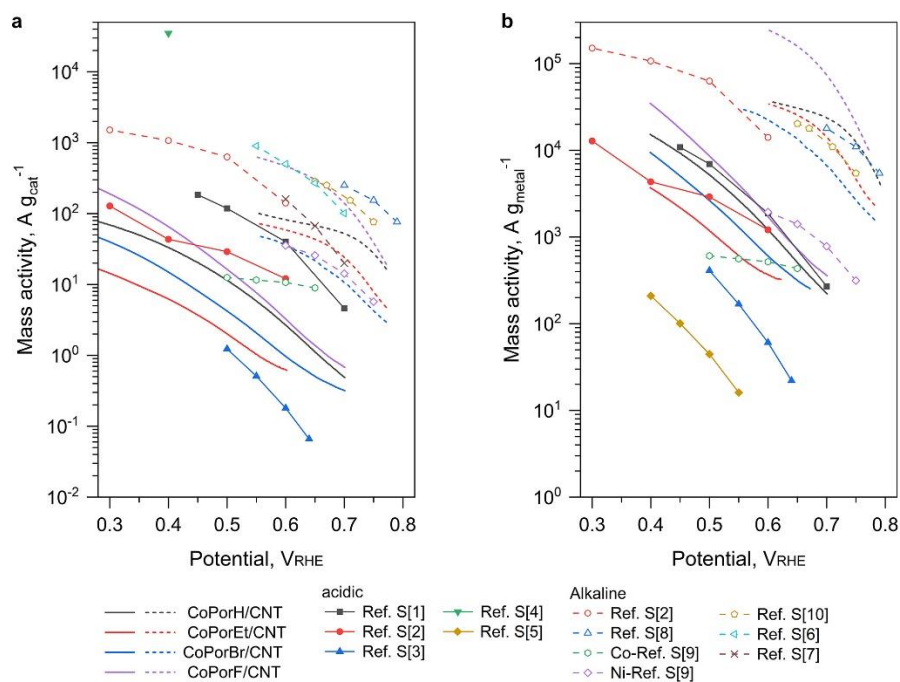
Figure S20. Mass activity of the HMCs in comparison to that of some recently reported catalysts. (a) Mass activity based on total catalyst mass. (b) Mass activity based on the mass of active metal. Reference data are listed in Table S8 and S9 below.
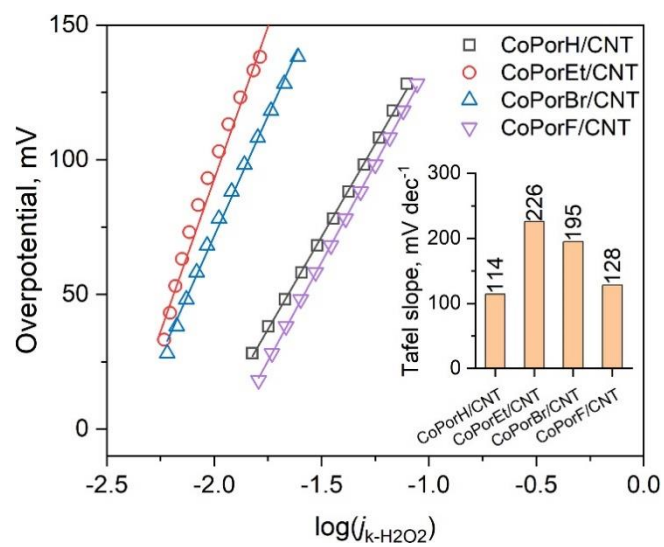
Figure S21. ORR Tafel plots of the catalysts obtained in an O_2 saturated 0.1 M $HClO_4$ electrolyte (pH=1.3).
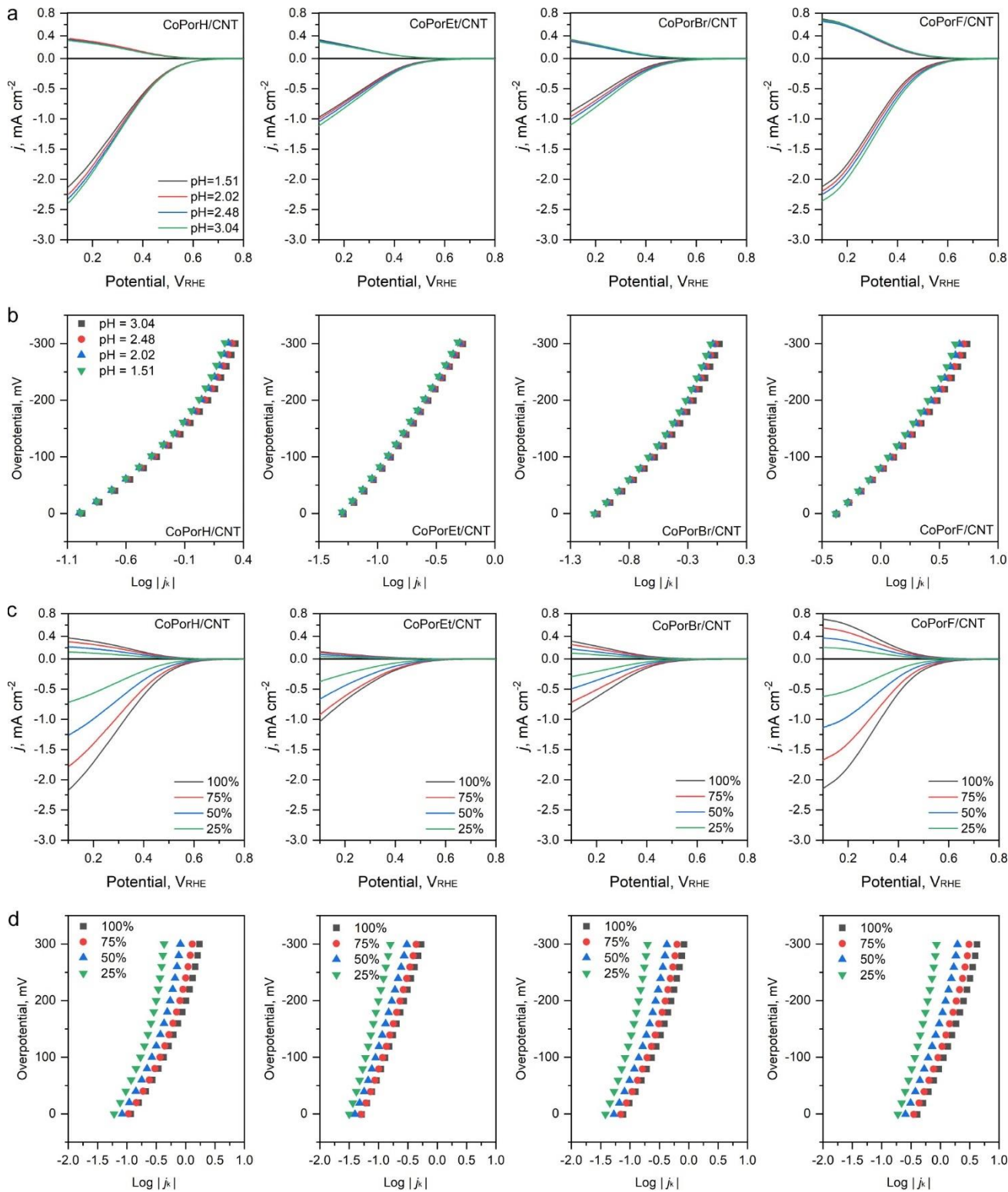
Figure S22. (a) LSV curves and (b) Tafel plots of the catalysts obtained at different pH values. (c) LSV curves and (d) Tafel plots of the catalysts obtained at different O_2 partial pressure.

23
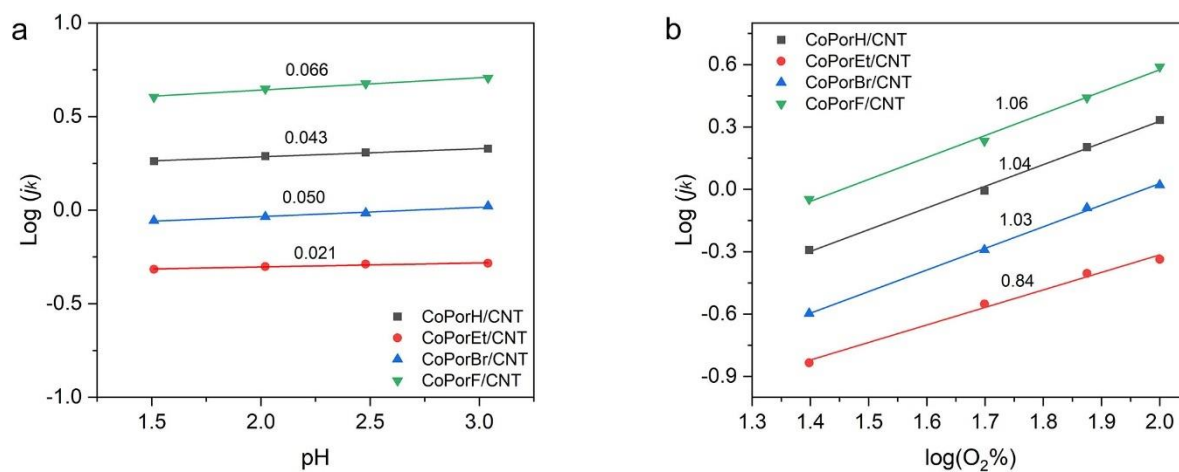
Figure S23. Reaction order of different catalysts against (a) H^+ concentration in terms of pH, and (b) O_2 concentration in terms of relative O_2 partial pressure ($\log(O_2\%)$). The H_2O_2-kinetic current density at an overpotential of 300 mV is used for fitting.
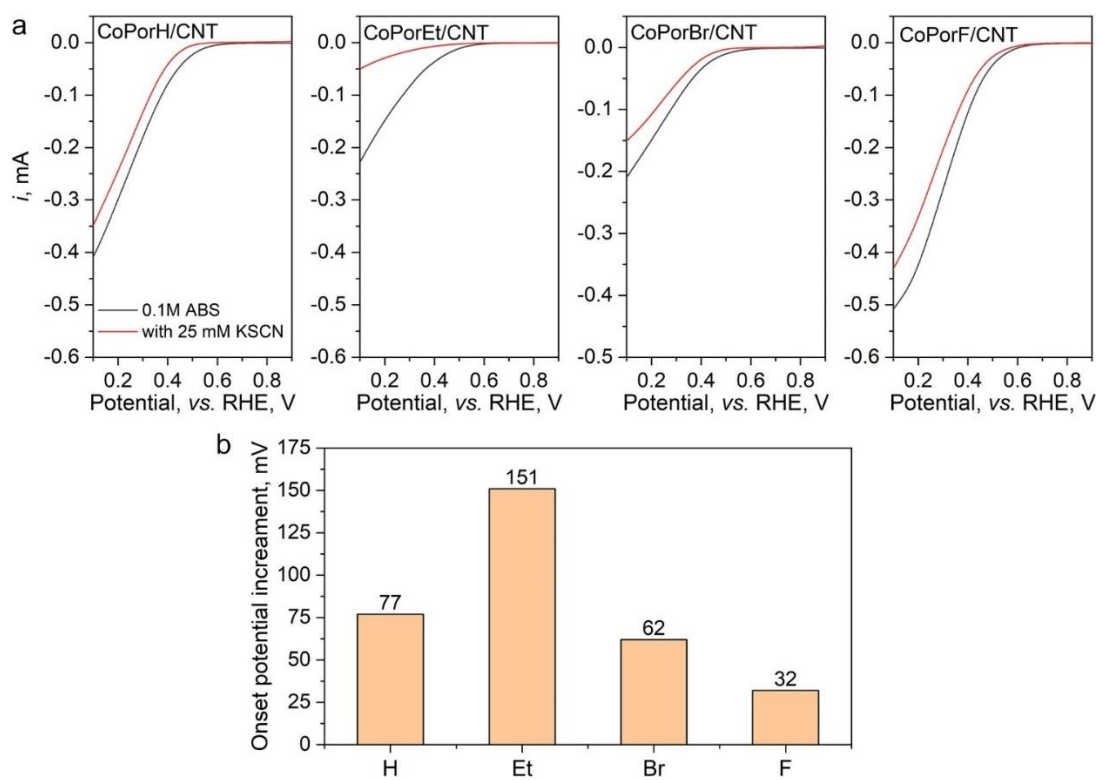
Figure S24. (a) LSV curves of the HMCs collected in O_2-saturated 0.1 M $HClO_4$ electrolyte with or without 25 mM KSCN. (b) Onset potential change of different HMCs.
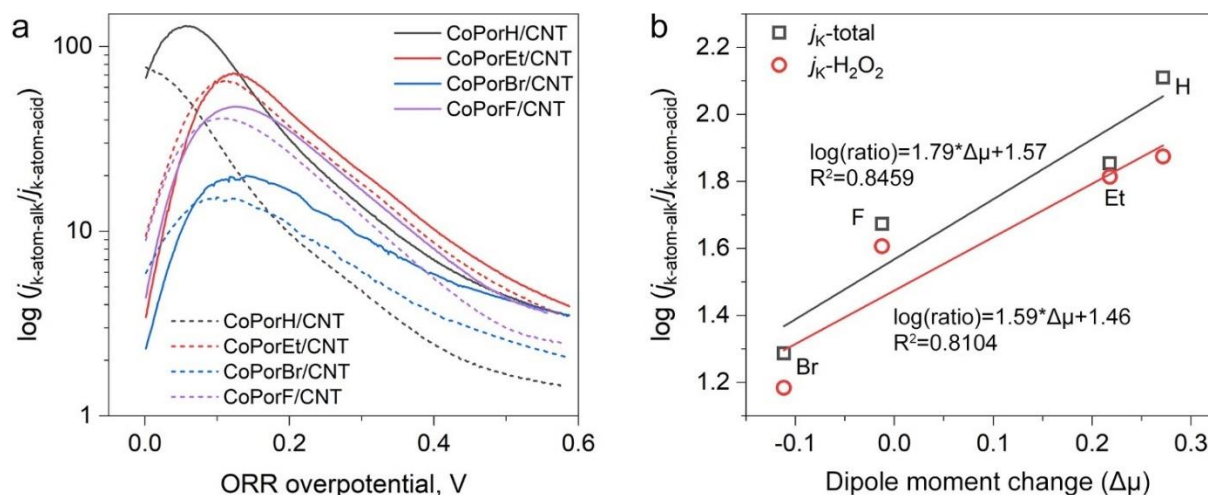
Figure S25. (a) Calculated performance enhancement in alkaline and acidic electrolytes based on the ratio between the per active site kinetic current ($j_{K\text{-alk-per atom}}$ and $j_{K\text{-acid per atom}}$) for total current (solid line) and H_2O_2 specific current (dashed line). (b) Correlation between the maximum performance enhancement (j_k ratio) to the dipole moment change (Table S10) of different HMCs.
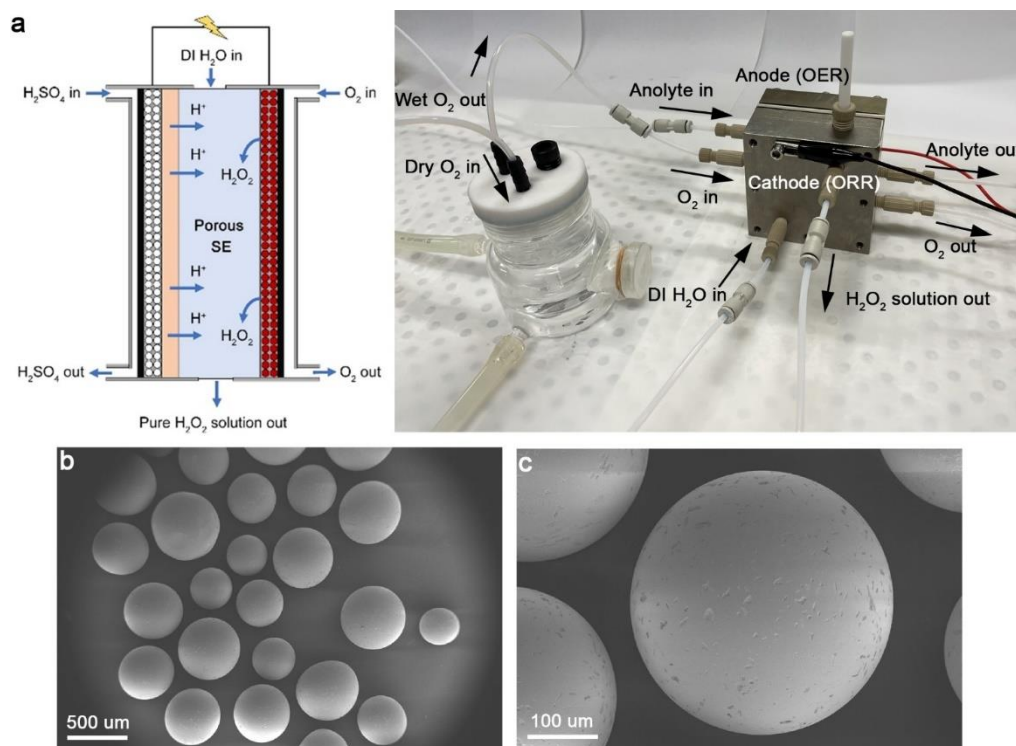
Figure S26. (a) A schematic illustration and a photo of the electrolyzer system. (b) and (c) SEM images of the solid-state electrolyte at different magnifications.
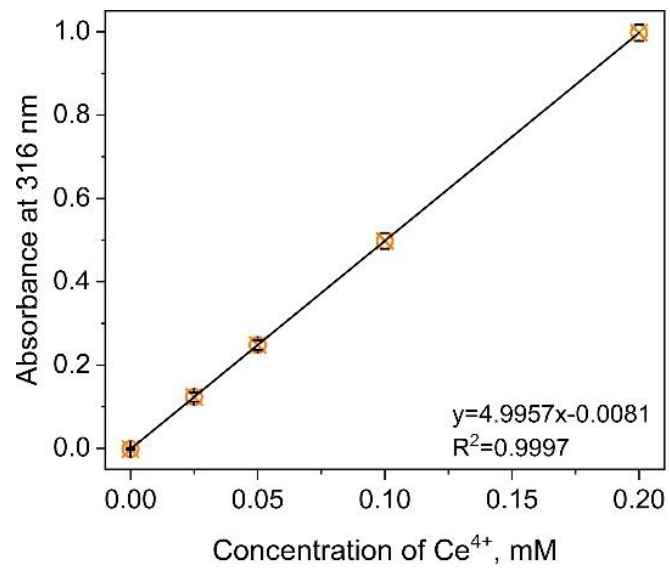
Figure S27. Calibration curve of the $Ce^{3+/4+}$ titration method.
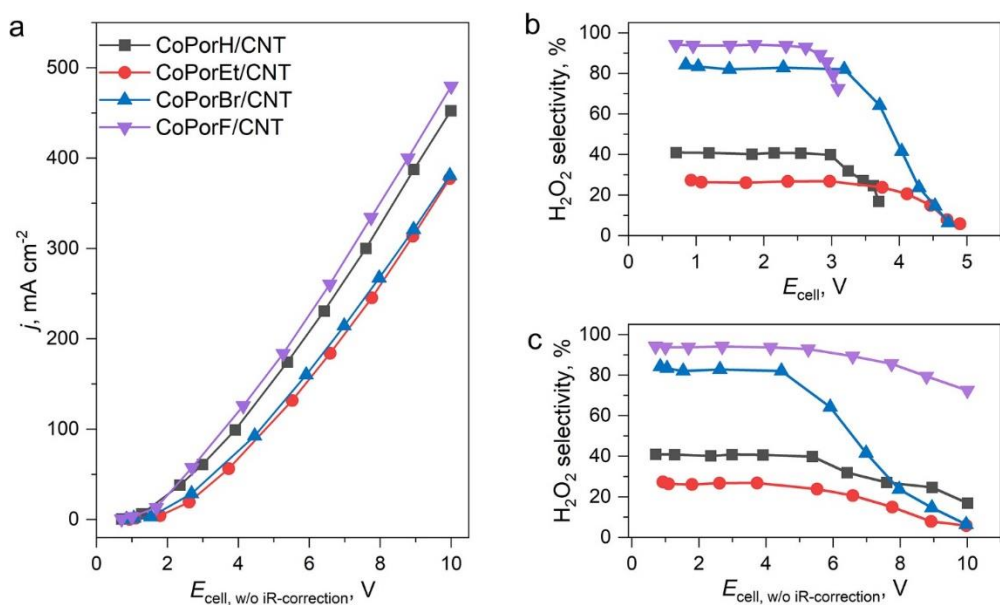
Figure S28. (a) Current-potential responses of the HMCs without iR-correction. H_2O_2 selectivity (molar fraction) of the HMCs at different cell voltages, (b) with and (c) without 80%-iR-correction.
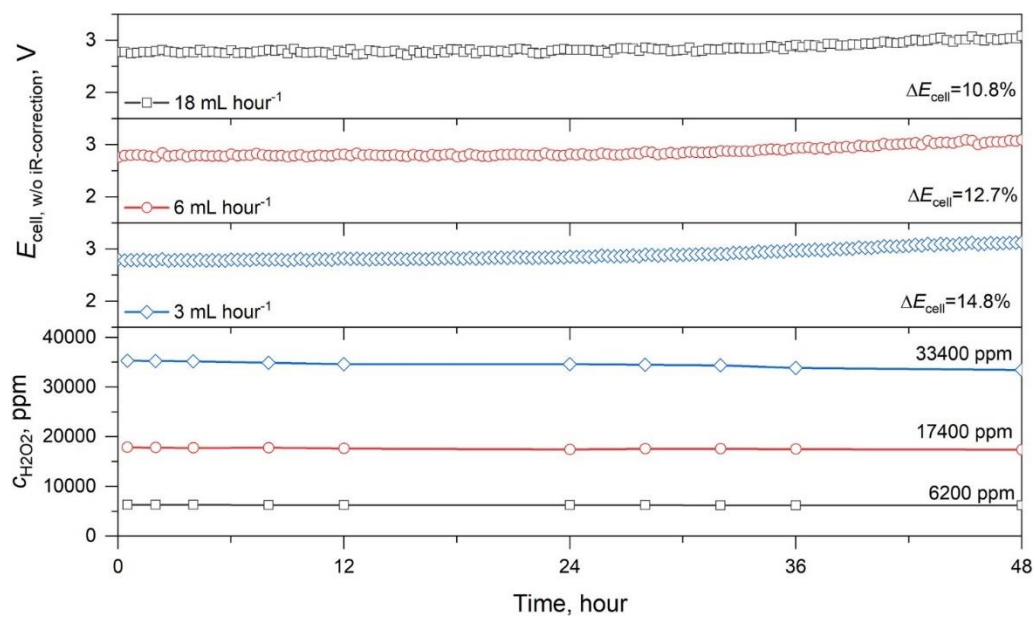
Figure S29. H_2O_2 concentration in products obtained at different H_2O flow rates in the electrolyzer with an electrode area of 4 cm^2, operating at 50 mA cm^{-2}.
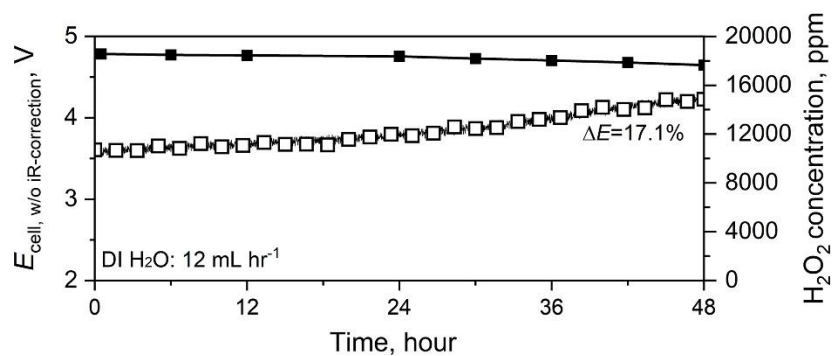
Figure S30. Stability performance and H_2O_2 concentration in products of CoPorF/CNT at 100 mA cm^{-2}.
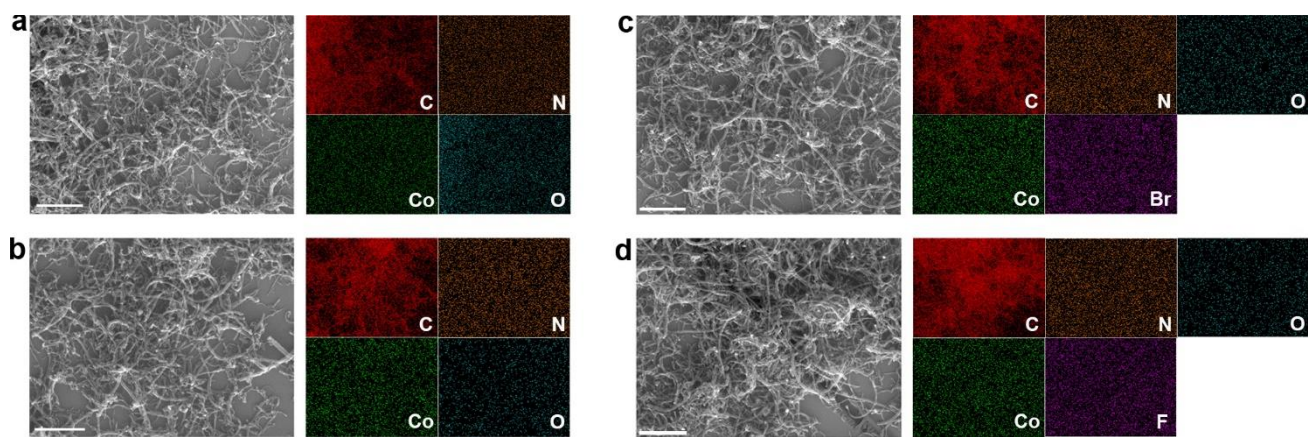
Figure S31. SEM images and corresponding EDX mapping results of (a) CoPorH/CNT, (b) CoPorEt/CNT, (c) CoPorBr/CNT, and (d) CoPorF/CNT. Scalebar corresponds to 1 µm.
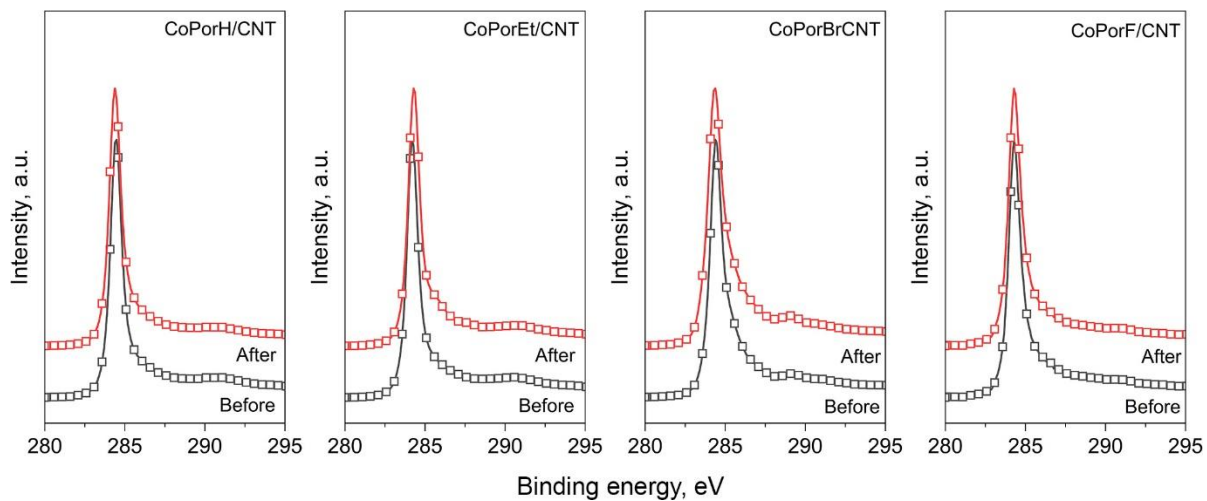
Figure S32. C 1*s* XPS spectra of the catalysts collected before and after the stability tests.
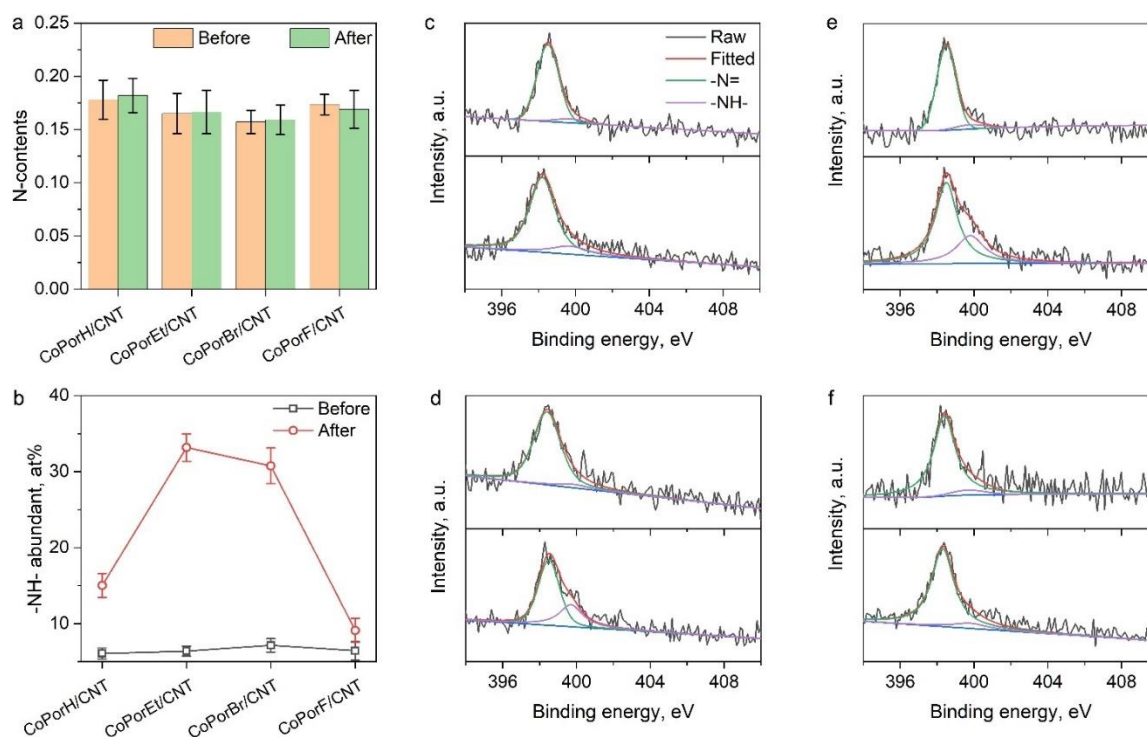
Figure S33. N 1s XPS spectra collected from the catalysts before and after stability tests. (a) N contents in the catalyst before and after discharging at 50 mA cm for 48 hours. (b) The atomic abundance of -NH- species (protonated N) in these samples, as determined by spectra deconvolution of (c) CoPorH/CNT, (d) CoPorEt/CNT, (e) CoPorBr/CNT, and (f) CoPorF/CNT. The spectra can be deconvoluted by two peaks, which can be assigned to the –N= that bonds to metal at 398.3 ± 0.1 eV) and protonated pyrrolic N (-NH-) at 399.7 ± 0.1 eV.
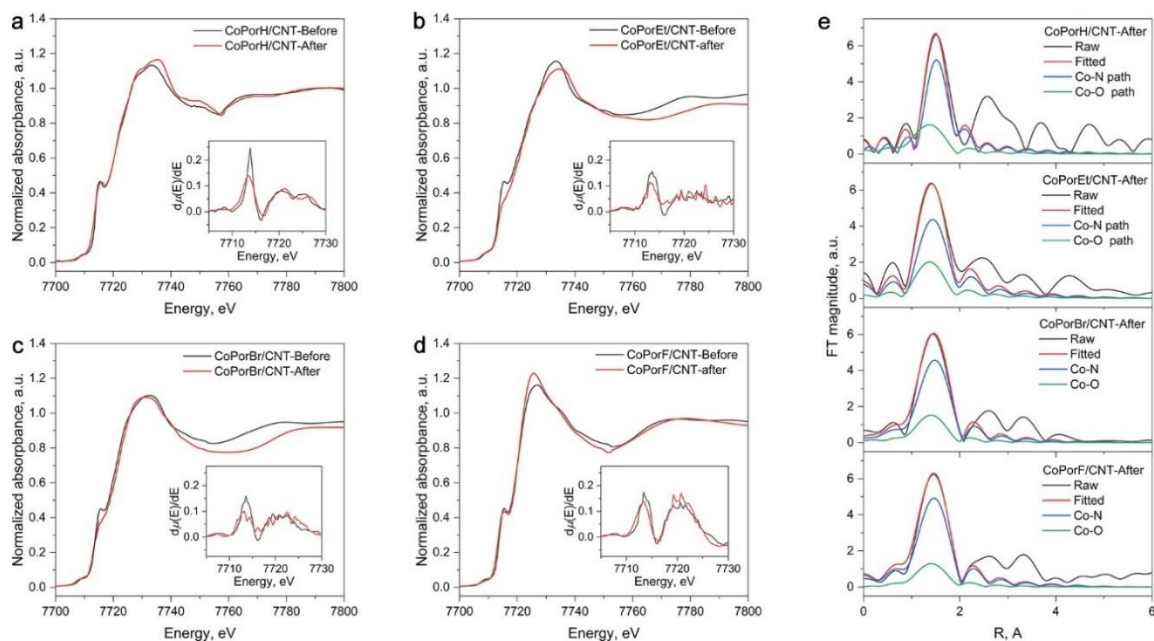
Figure S34. Comparison of Co K-edge XANES before and after stability test. (a) CoPorH/CNT, (b) CoPorEt/CNT, (c) CoPorBr/CNT and (d) CoPorF/CNT. (e) EXAFS spectra of the HMCs after stability test. The fitting results and parameters of the post-stability test spectra are listed in Table S10.
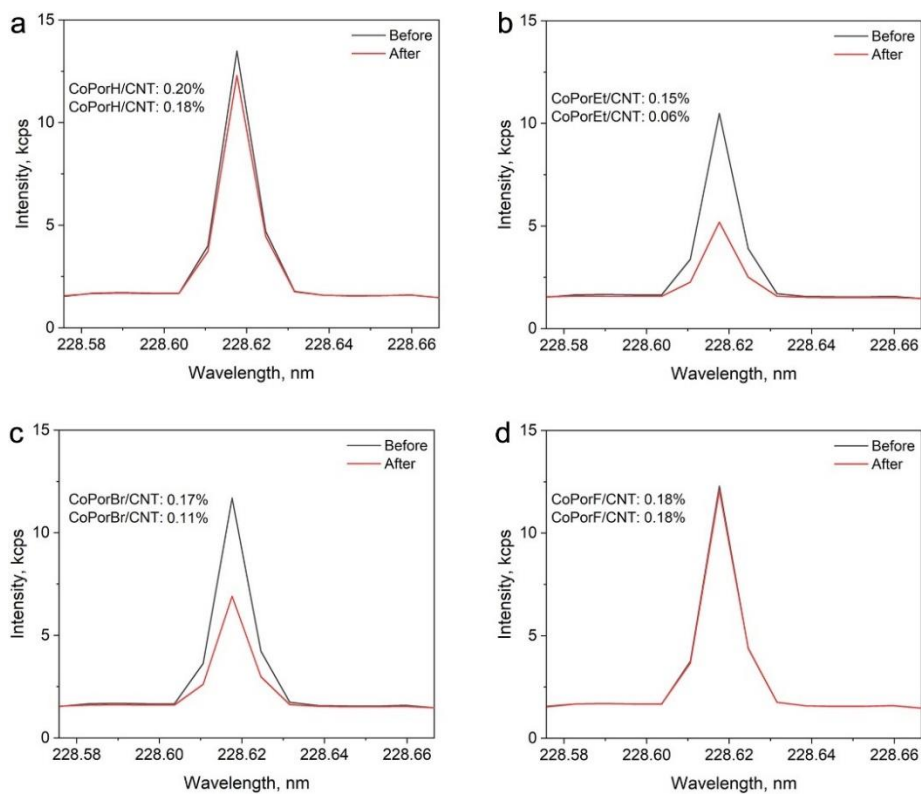
Figure S35. Co loading in the post-stability test catalysts determined by ICP-AES measurement of (a) CoPorH/CNT, (b) CoPorEt/CNT, (c) CoPorBr/CNT, and (d) CoPorF/CNT. The Co loss was 9%, 59%, 35%, and 2% for CoPorH/CNT, CoPorEt/CNT, CoPorBr/CNT and CoPorF/CNT, respectively.
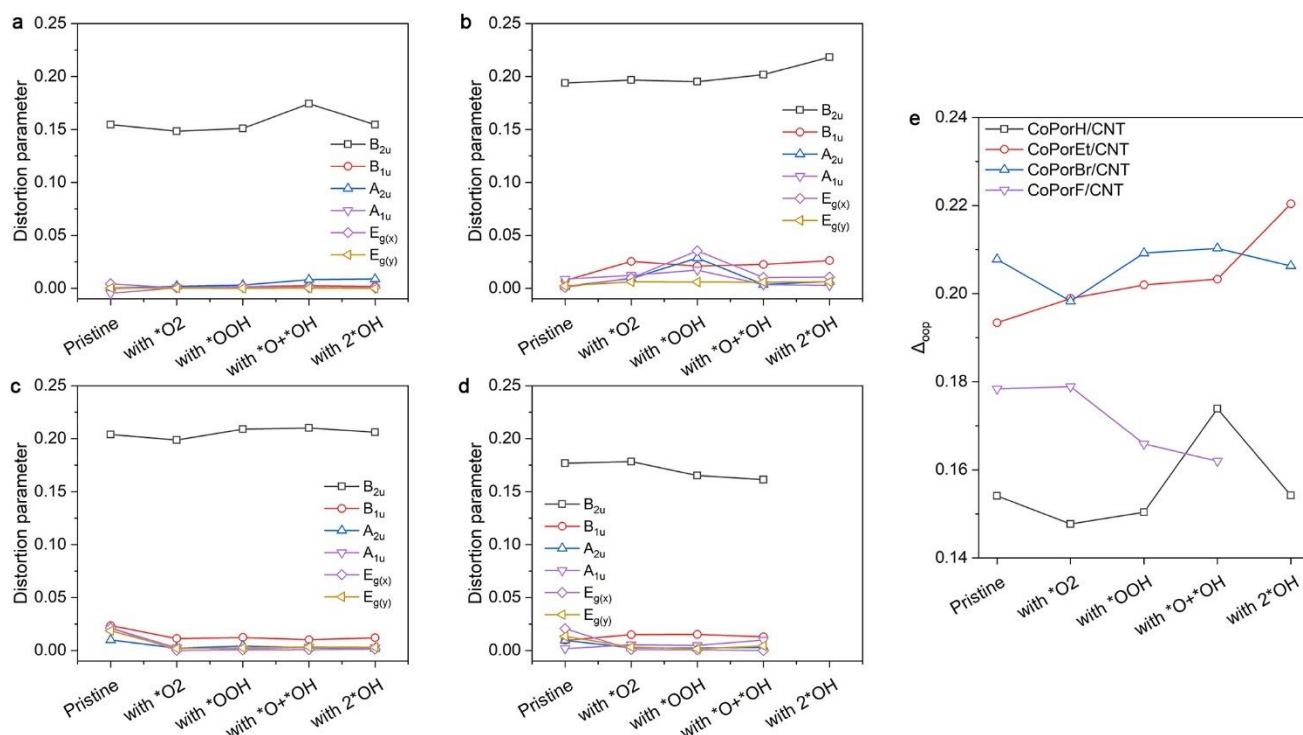
Figure S36. Porphyrin core confirmation distortion parameters of the HMCs with different oxygenous intermediate adsorbed. Coordinates were obtained from the geometry optimized models. Parameters were determined by the normal-coordinate structural decomposition method. All calculated DNMS properties of (a) CoPorH/CNT, (b) CoPorEt/CNT, (c) CoPorBr/CNT, and (d) CoPorF/CNT. (e) Comparison of the ΔOOP of the four HMCs at different reaction stages.
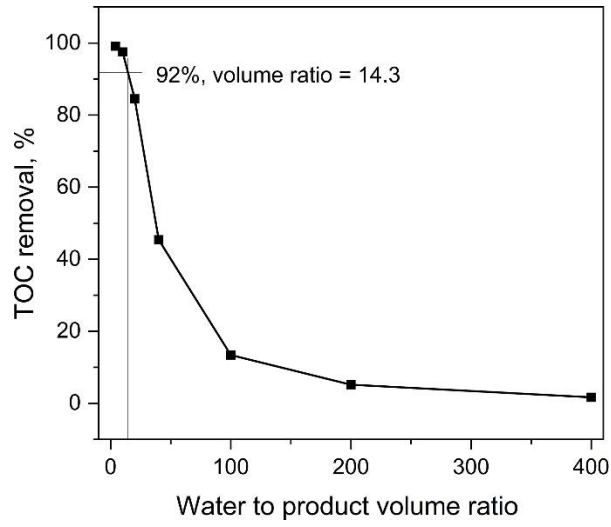
Figure S37. TOC removal rate as a function of groundwater to product volume ratio. The marked point corresponds to a removal rate of 92% or a 2ppm TOC residue.
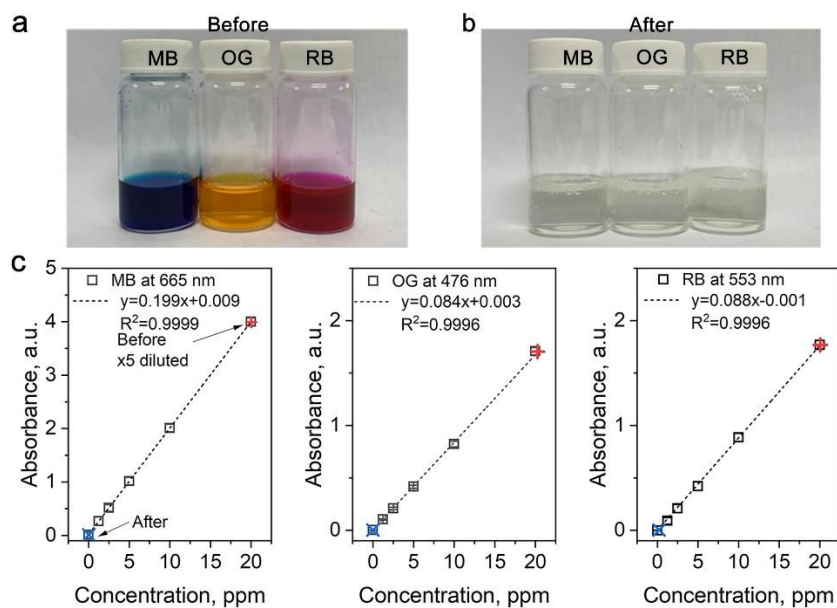
Figure S38. Organic dye removal capability of the H_2O_2 solution produced from the CoPorF/CNT catalyst-loaded electrolyzer. Photos of the 5 mL 100 ppm dye solutions (a) before and (b) after the addition of 1 mL H_2O_2 product were obtained at a flow rate of 6 mL hour^{-1} and a current density of 50 mA cm^{-2}. The solution was handshaked and kept still for 30 min. (c) The dye residues quantified by UV-vis absorption with their calibration curves.

Table S1. Calculated electronic properties of the porphyrins.

Sample	E_{LUMO+1}, eV	E_{LUMO}, eV	E_{HOMO}, eV	E_{HOMO-1}, eV	$\Delta E_{LUMO-HOMO}$, eV
H_2PorH	-2.29141	-2.46891	-5.29332	-5.55167	2.82441
H_2PorEt	-2.00100	-2.17286	-4.79667	-5.12663	2.62381
H_2PorBr	-3.23853	-3.29568	-5.86417	-6.08797	2.5685
H_2PorF	-2.96142	-3.10175	-6.02362	-6.28474	2.92186
CoPorH	-2.48612	-2.50355	-5.39322	-5.41211	2.88967
CoPorEt	-2.17117	-2.18066	-4.99236	-5.01722	2.81171
CoPorBr	-3.11337	-3.11391	-5.85668	-5.87858	2.74277
CoPorF	-3.1184	-3.13278	-6.07418	-6.09025	2.94140

Table S2. Calculated electronic spin moment of the cobalt atom in different porphyrins before and after adsorbing on the carbon substrate.

	$\mu_{before\ adsorption}$, μB	$\mu_{after\ adsorption}$, μB	$\Delta\mu$, μB
CoPorH	0.746	1.060	0.314
CoPorEt	0.795	1.010	0.215
CoPorBr	1.020	0.908	–0.112
CoPorF	0.007	1.019	1.012

Table S3. Calculated intermediate binding energy for H2O2 formation and the binding energy of thiocyanate (SCN) on different cobalt centers.

	E_{O2}, eV	E_{OOH}, eV	E_{HOOH}, eV	$\Delta E = E_{O2} - E_{HOOH}$, eV	E_{SCN}, eV
CoPorH/CNT	–0.75466	–1.28738	–0.36371	–0.39095	-1.72983
CoPorEt/CNT	–0.83818	–1.38657	–0.40096	–0.43722	-1.59957
CoPorBr/CNT	–0.49306	–1.11056	–0.20416	–0.2889	-1.52524
CoPorF/CNT	–0.58783	–1.21637	–0.25853	–0.3293	-1.60803

Table S4. Calculated Gibbs free energy of different elementary steps at U = 0V.

	CoPorH/CNT	CoPorEt/CNT	CoPorBr/CNT	CoPorF/CNT
*O_2	–0.11466	–0.19818	0.05217	0.14694
*OOH	–0.48588	–0.50156	–0.58171	–0.57067
*O + *OH	1.22421	1.30724	1.12868	1.10024
*O + H_2O	–2.80968	–2.88226	–2.77877	–2.66706
*OH + H_2O	–1.75893	–1.92706	–1.01894	–1.59475
$2H_2O$	–1.20788	–0.9418	–1.8243	–1.41556
*HOOH	–0.51613	–0.45419	–0.48196	–0.5334
2*OH	0.43947	0.39052	-	0.12156
*OH + H_2O	–3.26773	–3.43842	-	–2.74973
HOOH gas	–0.35626	–0.31901	–0.46144	–0.51581

Table S5. Spectroscopy properties of the porphyrins.

Substituents	Soret–peak		Bandgap change (exp./theo.), meV	Work function (with Co), eV
	Without Co, nm/eV	With Co, nm/eV		
H	413/3.002	410/3.024	22/65	4.71 ± 0.013
Et	455/2.725	432/2.870	145/187	4.62 ± 0.023
Br	467/2.655	449/2.762	107/174	4.84 ± 0.033
F	402/3.085	397/3.123	38/20	4.90 ± 0.028
CNT	-	-	-	5.05 ± 0.033

Table S6. Physiochemical properties of the HMCs

	Co loading, wt%	SSA, $m^2 g^{-1}$	Co K-edge EXAFS first shell fitting results				
			Co-N, Å	ΔR, Å	σ^2, $Å^{-2}$	ΔE_0, eV	R-factor
CoPorH/CNT	0.22	182 ± 3	1.943(5)	0.044(8)	0.00168	7.589	0.017
CoPorEt/CNT	0.17	177 ± 6	1.935(5)	-0.026(2)	0.00177	2.373	0.018
CoPorBr/CNT	0.16	174 ± 7	1.932(8)	-0.026(5)	0.00318	1.265	0.007
CoPorF/CNT	0.19	181 ± 4	1.939(0)	-0.025(6)	0.00338	1.462	0.011

Table S7. Porphyrin core confirmation distortion parameters as determined by the normal-coordinate structural decomposition method.

	basis	Δ_{oop}	B_{2u}	B_{1u}	A_{2u}	$E_g(x)$	$E_g(y)$	A_{1u}
CoPorH/CNT	min.	0.1541	0.1545	-0.0001	0.0003	-0.0048	0.0042	0.0003
CoPorEt/CNT	min.	0.1934	0.1938	0.0074	-0.0017	-0.0086	-0.0009	-0.0023
CoPorBr/CNT	min.	0.2078	0.2039	-0.0235	0.0099	-0.0212	0.0213	0.0187
CoPorF/CNT	min.	0.1784	0.1768	0.0096	0.0096	0.0018	0.0207	0.0134

Table S8. Performance of reported catalysts in acidic electrolytes (see Note 1 below).

In acidic electrolytes							
Catalyst	Metal loading, wt%	Catalyst loading, mg cm^{-2}	Potential, V_{RHE}	TOF, s^{-1}	Mass activity [b], A g^{-1}	Mass activity [c], A g$_{metal}^{-1}$	Ref.
CoPorF/CNT	0.19	0.01	0.48	3.51	22.01	11584	This work
Co-N-C(1)	1.7	0.025	0.7	0.083	4.59	270	Ref. S[1]
			0.6	0.48	31.99	1881	
			0.5	2.55	118.09	6946	
			0.45	4.62	184.60	10859	
Co-N-C(2)	1	0.1	0.6	0.369	12.08	1208	Ref. S[2]
			0.5	0.887	29.02	2902	
			0.4	1.325	43.33	4333	
			0.3	3.917	128.12	12812	
Co-Nx	0.3	1	0.64	0.007	0.066	22.10	Ref. S[3]
			0.6	0.019	0.18	60.71	
			0.55	0.051	0.51	168.4	
			0.5	0.125	1.23	410.0	
h-Pt$_1$-CuS$_x$	0.68 at%	0.1	0.4	0.060	35000	-	Ref. S[4]
Pt$_1$/SC [a]	2.5	-	0.55	0.016	-	16.07	Ref. S[5]
			0.5	0.045	-	44.57	
			0.45	0.102	-	100.8	
			0.4	0.212	-	209.7	

[a] The Pt loading on the electrode is set to 2.5 µg cm^{-2}. [b] Mass activity based on total catalyst mass. [c] Mass activity based on the mass of active metals.

Note 1

The TOF value and mass activity of these reported single-atom catalysts was either cited directly from their original publications or calculated based on the reported metal content in the catalysts and catalyst loadings on electrodes (as listed in Table S8). It should be noted that we assume all metal contents in these catalysts serve as single-atom active sites, as claimed in their original publications. The same calculation method was applied to the HMCs in this work. It should be noted that not all reported single-atom catalysts indeed only contain single-atom sites. Comparing them based on the same calculation method would give helpful information for readers to judge their catalytic activity. For carbon-based catalysts, the number of active sites was estimated based on oxygen content in the -C-O-C- configuration, which has been recognized as the key ORR active site.[6, 7] The mass activity of the reference catalysts were either directly used or calculated by using their extracted j_K values and the their reported catalyst loading and active element composition.

Table S9. Performance of reported catalysts in alkaline electrolytes.

Catalyst	Metal loading, wt%	Catalyst loading, mg cm^{-2}	Potential, V_{RHE}	TOF, s^{-1}	Mass activity [c], A g^{-1}	Mass activity [d], A g$_{metal}^{-1}$	Ref.
CoPorF/CNT	0.19	0.01	0.58	85.78	533.04	280546	This work
Co-N-C(3)	0.14	0.0375	0.79	1.224	76.23	5445	Ref. S[8]
			0.75	6.591	153.57	10969	
			0.70	29.116	250.75	17911	
Co-N-C(2)	1	0.1	0.60	0.369	140.60	14060	Ref. S[2]
			0.50	0.887	628.79	62879	
			0.40	1.325	1071.15	107115	
			0.30	3.917	1510.44	151044	
CoN$_x$/C-AQNH$_2$	2.06	0.1	0.65	0.171	8.94	434	Ref. S[9]
			0.60	0.186	10.66	518	
			0.55	0.195	11.55	561	
			0.50	0.211	12.51	607	
NiN$_x$/C-AQNH$_2$	1.82	0.1	0.75	0.096	5.71	314	
			0.70	0.239	14.22	781	
			0.65	0.432	25.69	1411	
			0.60	0.594	35.37	1943	
Co-NG(O)	1.4	0.01	0.75	1.665	76.23	5445	Ref. S[10]
			0.71	3.354	153.57	10969	
			0.67	5.476	250.75	17911	
			0.65	6.207	284	20286	
F-mrGO(600) [a]	6.5 at% [b]	0.01	0.7	0.0967	101	-	Ref. S[6]
			0.65	0.258	270	-	
			0.6	0.478	500	-	
			0.55	0.861	900	-	
O-CNT	8.8 at% [b]	0.101	0.7	0.0026	20	-	Ref. S[7]
			0.65	0.0088	67	-	
			0.6	0.021	160	-	

[a.] The catalyst was loaded on a porous electrode (AvCarb P50 carbon paper). [b] The active site density for carbon-based catalyst was estimated based on the XPS determined oxygen atomic percentage in the -C-O-C- configuration, which is recognized as ORR active site. [c.] Mass activity based on total catalyst mass. [d.] Mass activity based on the mass of active metals.

Table S10. The dipole moment of different Co centers.

	Dipole with O adsorption	Dipole without adsorption	Dipole moment change
CoPorH/CNT	0.303	0.031	0.272
CoPorEt/CNT	-0.191	-0.408	0.218
CoPorBr/CNT	0.308	0.419	-0.112
CoPorF/CNT	0.347	0.360	-0.013

Table S11. EXAFS fitting results of the post-stability test catalysts.

	Path	CN	Bond length, Å	ΔR, Å	σ^2, Å^{-2}	ΔE_0, eV	R-Factor
CoPorH/CNT	Co–N	3.84(3)	1.941(9)	0.033(0)	0.00113	6.614	0.014
	Co–O	0.42(8)	1.899(4)	0.028(9)	0.00094	6.722	0.009
CoPorEt/CNT	Co–N	3.22(7)	1.966(5)	-0.028(4)	0.00223	5.800	0.019
	Co–O	0.70(2)	1.863(6)	0.035(0)	0.00797	6.899	0.003
CoPorBr/CNT	Co–N	3.41(9)	1.951(4)	-0.038(7)	0.00739	3.319	0.005
	Co–O	0.61(5)	1.892(4)	0.044(8)	0.00804	2.623	0.002
CoPorF/CNT	Co–N	3.93(2)	1.957(9)	-0.004(3)	0.01317	-4.840	0.018
	Co–O	0.32(1)	1.911(0)	0.047(3)	0.01126	-4.063	0.017

Reference

1. Gao, J., et al., *Enabling Direct H₂O₂ Production in Acidic Media through Rational Design of Transition Metal Single Atom Catalyst.* Chem, 2020. **6**(3): p. 658-674.
2. Sun, Y., et al., *Activity–Selectivity Trends in the Electrochemical Production of Hydrogen Peroxide over Single-Site Metal–Nitrogen–Carbon Catalysts.* J. Am. Chem. Soc., 2019. **141**(31): p. 12372-12381.
3. Yamanaka, I., et al., *Electrocatalysis of Heat-Treated Cobalt-Porphyrin/carbon for Hydrogen Peroxide Formation.* Electrochim. Acta, 2013. **108**: p. 321-329.
4. Shen, R., et al., *High-Concentration Single Atomic Pt Sites on Hollow CuSₓ for Selective O₂ Reduction to H₂O₂ in Acid Solution.* Chem, 2019. **5**(8): p. 2099-2110.
5. Choi, C.H., et al., *Tuning Selectivity of Electrochemical Reactions by Atomically Dispersed Platinum Catalyst.* Nat. Commun., 2016. **7**(1): p. 10922.
6. Kim, H.W., et al., *Efficient hydrogen peroxide generation using reduced graphene oxide-based oxygen reduction electrocatalysts.* Nat. Catal., 2018. **1**(4): p. 282-290.
7. Lu, Z., et al., *High-efficiency oxygen reduction to hydrogen peroxide catalysed by oxidized carbon materials.* Nat. Catal., 2018. **1**(2): p. 156-162.
8. Gong, H., et al., *Low-Coordinated Co-N-C on Oxygenated Graphene for Efficient Electrocatalytic H₂O₂ Production.* Adv. Funct. Mater., 2022. **32**(5): p. 2106886.
9. Li, X., et al., *Molecule Confined Isolated Metal Sites Enable the Electrocatalytic Synthesis of Hydrogen Peroxide.* Adv. Mater., 2022. **34**(25): p. 2104891.
10. Jung, E., et al., *Atomic-Level Tuning of Co–N–C Catalyst for High-Performance Electrochemical H₂O₂ Production.* Nat. Mater., 2020. **19**(4): p. 436-442.